J. Fluid Mech. (2010), *vol.* 657, *pp.* 361–393.
doi:10.1017/S0022112010001710

Direct numerical simulation of transonic shock/boundary layer interaction under conditions of incipient separation

SERGIO PIROZZOLI†, MATTEO BERNARDINI AND FRANCESCO GRASSO

Dipartimento di Meccanica e Aeronautica, Università di Roma 'La Sapienza', Via Eudossiana 18, 00184 Rome, Italy

(Received 1 October 2009; revised 2 April 2010; accepted 6 April 2010; first published online 24 June 2010)

The interaction of a normal shock wave with a turbulent boundary layer developing over a flat plate at free-stream Mach number $M_\infty = 1.3$ and Reynolds number $Re_\theta \approx 1200$ (based on the momentum thickness of the upstream boundary layer) is analysed by means of direct numerical simulation of the compressible Navier–Stokes equations. The computational methodology is based on a hybrid linear/weighted essentially non-oscillatory conservative finite-difference approach, whereby the switch is controlled by the local regularity of the solution, so as to minimize numerical dissipation. As found in experiments, the mean flow pattern consists of an upstream fan of compression waves associated with the thickening of the boundary layer, and the supersonic region is terminated by a nearly normal shock, with substantial bending of the interacting shock. At the selected conditions the flow does not exhibit separation in the mean. However, the interaction region is characterized by 'intermittent transitory detachment' with scattered spots of instantaneous flow reversal throughout the interaction zone, and by the formation of a turbulent mixing layer, with associated unsteady release of vortical structures. As found in supersonic impinging shock interactions, we observe a different amplification of the longitudinal Reynolds stress component with respect to the others. Indeed, the effect of the adverse pressure gradient is to reduce the mean shear, with subsequent suppression of the near-wall streaks, and isotropization of turbulence. The recovery of the boundary layer past the interaction zone follows a quasi-equilibrium process, characterized by a self-similar distribution of the mean flow properties.

Key words: compressible boundary layers, shock waves, turbulence simulation

1. Introduction

The interaction of shock waves with turbulence is the subject of extensive research for its relevance in transonic, supersonic and hypersonic flows. In the transonic regime, shock wave/turbulent boundary layer interactions (SBLIs) occur in a variety of flows of practical interest, such as high-speed wings, helicopter blades, turbo-machines, over-expanded nozzles, launch vehicles during the ascent phase, etc. A fundamental understanding of the complex physical phenomena involved in such interactions is

† Email address for correspondence: sergio.pirozzoli@uniroma1.it

extremely important for the development of improved engineering models and to attempt to control their detrimental effects. SBLI may indeed be responsible for loss of efficiency of aerodynamic surfaces, for structural fatigue and severe structural vibrations associated with unsteady pressure loads, especially in the presence of flow separation. Models of flow-induced vibration require accurate prediction of frequency/wavenumber spectra of wall-pressure fluctuations as a forcing input, which can be achieved by means of high-fidelity unsteady numerical simulations.

Significant advances in the understanding of SBLI have been made in the past few decades, even though the associated unsteady features and the turbulence-amplification mechanisms are not yet fully understood. This is especially true for transonic interactions, which have received comparatively less attention with respect to their supersonic counterparts, such as impinging shocks and compression ramps (Dolling 2001). The major problems derive from the difficulties encountered in both experiments and computations in anchoring the shock wave and from the strong sensitivity to the downstream (subsonic) flow conditions.

Délery & Marvin (1986), through the analysis of a large amount of experimental information related to quasi-normal shock/boundary layer interactions in several configurations (including airfoils, nozzles, bumps), have identified two regimes: (i) weak interactions, where the flow is not separated in the mean, and (ii) strong interactions, which are characterized by significant flow separation. In the former case the shock pattern consists of a fan of compression waves that arise upstream of the nominal shock impingement point and is terminated by a quasi-normal 'rear' shock, which generally brings the flow to subsonic conditions. In the latter case, the compression waves coalesce to form a leading shock, and a region of supersonic flow is observed past the rear shock, called a 'supersonic tongue' (Seddon 1960). The intersection of the leading shock with the rear shock causes the formation of a slip line, and the so-called lambda shock pattern is observed. The general consensus is that, regardless of the Reynolds number, incipient mean flow separation occurs when the upstream Mach number is $M_0 \approx 1.3$. Indeed, as explained by Délery & Marvin (1986), as the Reynolds number decreases, the interaction length scale increases, and the compression is spread over a longer distance, thus delaying the separation.

Transonic SBLI in a channel with a wall-mounted bump were experimentally investigated by Délery (1983) (some data, which will be used in the paper, were also reported in Délery & Marvin 1986), who considered shock strengths in the range $M_0 = 1.3$–1.45 and $Re_{\theta_0} \approx 3000$–$7500$ (Re_{θ_0} being the Reynolds number based on the momentum thickness at the origin of the interaction), corresponding to conditions from incipient separation to extensively separated flow. The experiments showed a differential amplification of the Reynolds stress components, whose maxima were found to occur well away from the wall. The experiments also revealed the occurrence of a relaxation process on a very long spatial scale, associated with the persistence of the vortical structures that are formed through the interaction. Atkin & Squire (1992) experimentally investigated the steady interaction of a normal shock wave with a turbulent boundary layer in a straight rectangular channel in the Mach number range $M_0 = 1.3$–1.55 at $Re_{\theta_0} \approx 10^4$. The wall pressure was found to increase starting from approximately $5\,\delta_0$ (δ_0 being the thickness at the origin of the interaction) ahead of the shock, and it levelled off to the value predicted by the Rankine–Hugoniot jump relations at about $70\,\delta_0$ past the interacting shock.

Bruce (2008) and Bruce & Babinsky (2008) have carried out an experimental campaign on forced and unforced transonic SBLI in a rectangular channel, both with and without control. The steady data at $M_0 = 1.3$, $Re_{\theta_0} \approx 10^4$ show a pattern

typical of a weak SBLI, with a compression fan ahead of the main shock, attached flow throughout the interaction region and the presence of a small supersonic tongue, associated with recovery shocklets.

A wide body of research on the solution of Reynolds-averaged Navier–Stokes (RANS) equations is available for a broad variety of flows involving shock wave/boundary layer interactions, for both two- and three-dimensional configurations (Davidson 1995; Gerolymos & Vallet 1997; Batten *et al.* 1999; Barakos & Drikakis 2000; Leschziner, Batten & Loyau 2000; Leschziner & Drikakis 2002). As a general conclusion, these studies have shown the ability of turbulence models to capture the mean flow features (such as the pressure loads and the extent of the interaction region). This is particularly true for second-moment closures, where the anisotropy is directly taken into account by solving the full Reynolds stress transport equations. Despite these encouraging results, efforts are still needed to improve turbulence models, especially for predicting the rapid rise and subsequent decay of turbulence in the separated shear layer developing past the interacting shock (Knight *et al.* 2003; Sandham, Yao & Lawal 2003).

A very limited number of three-dimensional large-eddy simulations (LES) of transonic SBLI have been reported so far. Sandham *et al.* (2003) performed LES (based on the dynamic Smagorinsky model and a synthetic turbulence technique to force transition to turbulent state) of a transonic turbulent boundary layer over a circular-arc bump corresponding to an upstream Mach number $M_0 \approx 1.16$. These authors concluded that the shock wave is very nearly steady, and the level of turbulence anisotropy in the flow past the interaction is not substantial. Significant differences (earlier flow separation, lower peak Mach number) from reference experiments (Liu & Squire 1988) were reported.

A preliminary attempt to perform a direct numerical simulation (DNS) of transonic SBLI was undertaken by the present authors (Pirozzoli, Bernardini & Grasso 2007), who analysed the interaction of a normal shock wave with a supersonic turbulent boundary layer flow at $M_\infty = 1.2$, $Re_\theta \approx 800$, and found qualitative association between the amplification of turbulence and noise, and the formation of eddies past the interaction zone. A quantitative analysis of the pressure field also showed a relation between the local r.m.s. wall pressure and the maximum Reynolds shear stress in the wall-normal direction.

The objective of this paper is to investigate transonic SBLI by means of DNS of the full governing equations. The study focuses in particular on the analysis of the unsteadiness associated with the development of the vortical structures in the boundary layer, rather than on the low-frequency unsteadiness that may result from self-sustained oscillations (global modes) or with time variation of boundary conditions. To the authors' knowledge, no other DNS studies of transonic interactions have appeared in the literature so far. DNS has the capability to provide insight into the full range of turbulence flow scales and furnish information on any quantity of interest, like second-moment budgets. Therefore, we expect that the present simulation can help turbulence modellers by providing a reliable database for the development of improved models for compressible flows with turbulence out of equilibrium. To make our analysis as general as possible, we consider a relatively simple geometrical set-up, whereby the turbulent boundary layer developing over a flat surface is made to interact with a nominally normal shock wave. This type of interaction has the merit of isolating the effect of bulk flow compression, thus alleviating the complicating effect due to streamline curvature, which may lead to the onset of Goertler instabilities. A normal shock wave with moderate strength ($M_\infty = 1.3$)

is considered, which nominally corresponds to a condition of incipient mean flow separation.

This paper is organized as follows. The numerical methodology is described in § 2; the results of the study are presented in § 3, which includes a quantitative analysis of the mean and statistical properties of the flow field. Concluding remarks are given in § 4.

2. Numerical strategy

In this paper, we solve the full three-dimensional unsteady Navier–Stokes equations for a perfect gas cast in conservation form:

$$\left.\begin{aligned} \frac{\partial \rho}{\partial t} + \frac{\partial (\rho u_j)}{\partial x_j} &= 0, \\ \frac{\partial (\rho u_i)}{\partial t} + \frac{\partial (\rho u_i u_j)}{\partial x_j} + \frac{\partial p}{\partial x_i} - \frac{\partial \sigma_{ij}}{\partial x_j} &= 0, \\ \frac{\partial (\rho E)}{\partial t} + \frac{\partial (\rho E u_j + p u_j)}{\partial x_j} - \frac{\partial (\sigma_{ij} u_i - q_j)}{\partial x_j} &= 0, \end{aligned}\right\} \tag{2.1}$$

where ρ is the density, u_i is the velocity component in the ith coordinate direction ($i = 1, 2, 3$), p is the thermodynamic pressure, and

$$\left.\begin{aligned} q_j &= -k \frac{\partial T}{\partial x_j}, \\ \sigma_{ij} &= 2 \mu S_{ij} - \tfrac{2}{3} \mu S_{kk} \delta_{ij} \end{aligned}\right\} \tag{2.2}$$

are the heat flux vector and the viscous stress tensor, respectively, and $S_{ij} = (u_{i,j} + u_{j,i})/2$ is the rate of strain tensor. The molecular viscosity is assumed to obey Sutherland's law, and the thermal conductivity is related to μ through the relation $k = c_p \mu / Pr$ (the molecular Prandtl number is assumed to be 0.72). In the analysis that follows the instantaneous-flow-field variables are decomposed using either the standard Reynolds decomposition ($f = \overline{f} + f'$) or the density-weighted (Favre) decomposition ($f = \tilde{f} + f''$), where $\tilde{f} = \overline{\rho f}/\overline{\rho}$.

The computational strategy to solve the governing equations is a modification of a conservative finite-difference approach that has been extensively validated in previous works both for isotropic decaying compressible turbulence and for wall-bounded turbulent supersonic flows (Pirozzoli & Grasso 2004, 2006). In the smooth parts of the flow field the inviscid fluxes are discretized by means of a linear seventh-order central upstream approximation exploiting local Lax–Friedrichs flux splitting, whereas a fifth-order weighted essentially non-oscillatory (WENO) reconstruction (Jiang & Shu 1996) is activated near shock transitions to inhibit spurious Gibbs oscillations. As proposed by Pirozzoli (2002), the switch between linear and WENO reconstruction is carried out at the intermediate nodes of the computational mesh on the basis of the value of the density difference across the neighbouring nodes ($\Delta\rho_{j+1/2} = \rho_{j+1} - \rho_j$). In particular, the WENO reconstruction is activated whenever the absolute value of the density difference becomes larger than a suitable threshold value $\Delta\rho^*$, defined as

$$\frac{\Delta\rho^*}{\rho_\infty} = \varepsilon_1 + \frac{\varepsilon_2 - \varepsilon_1}{1 + M^{20}}, \tag{2.3}$$

where M is the local Mach number, and the constants are set to $\varepsilon_1 = 0.01$, $\varepsilon_2 = 0.5$. To avoid spurious shock detection, a low threshold level ($\Delta\rho^*/\rho_\infty = \varepsilon_1$) is used in the supersonic part of the flow field, whereas a larger threshold ($\Delta\rho^*/\rho_\infty = \varepsilon_2$) is

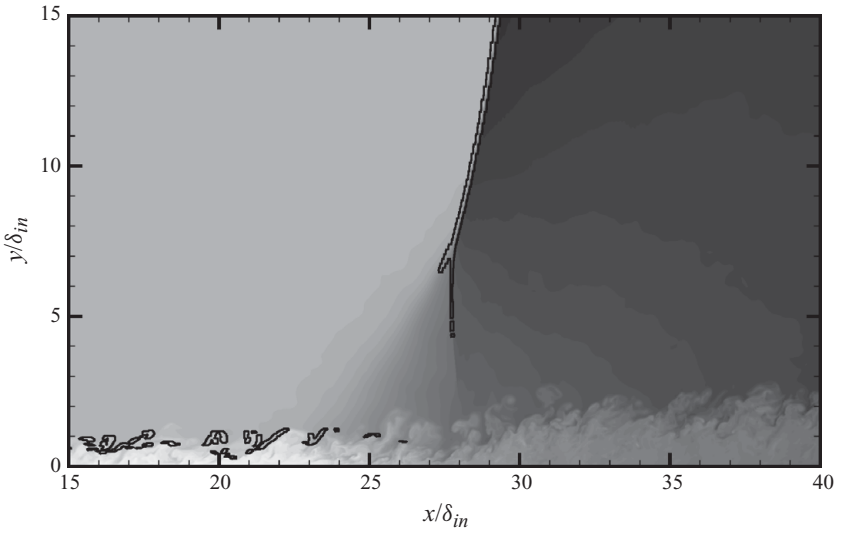

FIGURE 1. Assessment of shock sensor. Points where $|\Delta\rho| > \Delta\rho^*$ are marked as solid lines and are overlaid on flooded instantaneous density contours ($0.75 \leqslant \rho/\rho_\infty \leqslant 1.55$, 40 contours).

used in the subsonic part of the boundary layer (which does not support shock transitions). Such a procedure guarantees that the high-order linear reconstruction is used throughout the subsonic layer, while the more dissipative shock-capturing reconstruction is selectively applied to a very limited number of grid points, as shown in figure 1.

The viscous fluxes are approximated by means of standard second-order central differences, and time integration is performed by means of a classical four-stage fourth-order explicit Runge–Kutta algorithm.

2.1. *Computational domain*

The computational domain employed for the simulation is schematically depicted in figure 2. The choice of the streamwise extent (L_x) is dictated by the necessity to accommodate the entire interaction zone, including a large part of the recovery region past the impinging shock. The selection of the extent in the wall-normal direction (L_y) is critical to avoid drift of the shock system induced by pressure disturbances coming from the downstream subsonic part of the domain, and this may prevent the achievement of a statistically steady state. The size of the computational domain in the spanwise direction (L_z) has to guarantee that the two-point correlations of all flow variables fall off sufficiently fast so as not to cause any spurious dynamics. The computational domain, whose size ($L_x \times L_y \times L_z = 106.8\delta_{in} \times 427\delta_{in} \times 12.8\delta_{in}$, where δ_{in} is the inflow boundary-layer thickness based on the 99 % free-stream velocity) has been selected through a series of preliminary calculations, is discretized with a grid consisting of $2561 \times 281 \times 351$ points. The grid points are uniformly spaced in the spanwise direction, whereas they are mildly clustered in the streamwise direction around the nominal location of the normal shock wave ($x_s = 32\,\delta_{in}$). The well-resolved part of the computational domain extends up to $x = 64\,\delta_{in}$, and an algebraic mapping is used to progressively stretch the mesh up to the outflow boundary. Grid points are clustered in the wall-normal direction according to a hyperbolic sine mapping up to $y/\delta_{in} = 8.5$, and then a geometric progression is used up to the upper boundary of the computational domain. In wall units (based on the friction velocity $u_\tau = \sqrt{\tau_w/\rho_w}$ and

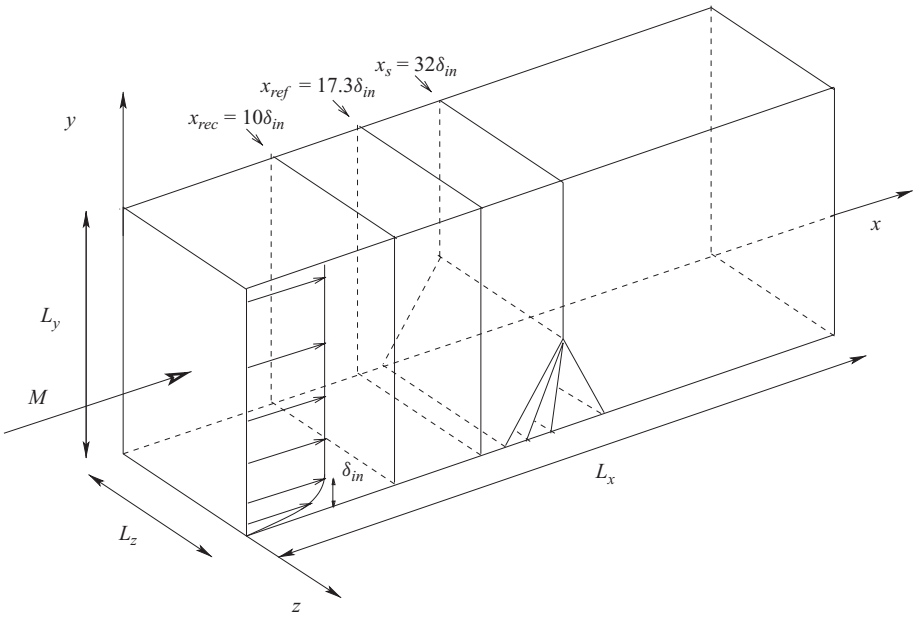

FIGURE 2. Sketch of the computational domain for the analysis of normal shock wave/boundary layer interaction (axes not to scale). The variable x_{rec} denotes the recycling station; x_{ref} is the reference station used for normalization; x_s is the nominal shock location; δ_{in} is the boundary-layer thickness (based on the 99 % free-stream velocity) at the inflow.

the viscous length scale $\delta_v = \nu_w/u_\tau$, evaluated immediately upstream of the interaction zone), the streamwise spacing (Δx^+) varies between 4.5 and 7.5; the spacing in the wall-normal direction (Δy^+) ranges between 1.1 at the wall and 20.1 at $y/\delta_{in} = 8.5$, and the spanwise mesh spacing is $\Delta z^+ = 5.53$. The ratio of the effective mesh spacing, $\Delta = (\Delta x \cdot \Delta y \cdot \Delta z)^{1/3}$, to the local Kolmogorov length scale $\eta = \sqrt{\overline{\rho}}^{-1/2}\overline{\mu}^{3/4}(\overline{\sigma'_{ij}\, u'_{i,j}})^{1/4}$, is checked *a posteriori* to be less than 4.3 throughout the interaction zone.

As shown by Jiménez & Wray (1998) for isotropic turbulence, and confirmed by Pirozzoli, Bernardini & Grasso (2008) for wall turbulence, the typical size of the small-scale eddies is (5–6)η, which indicates that all the scales of turbulent motion are expected to be adequately resolved in the present simulation. This is further confirmed by the inspection of the energy budgets, to be reported in figure 27. The distribution of the two-point correlation coefficient of the velocity components is reported in figure 3 as a function of the spanwise separation (r_z) at a station downstream of the shock. The data reported in the figure do not suggest the occurrence of any apparent spurious coherence.

2.2. *Boundary and initial conditions*

A critical issue in the simulation of shock/boundary layer interactions is the prescription of suitable inflow conditions to guarantee a fully developed turbulent state of the boundary layer at the shortest possible distance from the inflow. In the present DNS this is achieved by exploiting a modified version of the original rescaling–recycling procedure developed by Lund, Wu & Squires (1998), and extended to the compressible case by Stolz & Adams (2003) and Xu & Martin (2004). The basic idea consists of extracting a cross-stream slice of the flow field and recycling it to the inflow, after suitable rescaling. This approach produces a realistic turbulent boundary

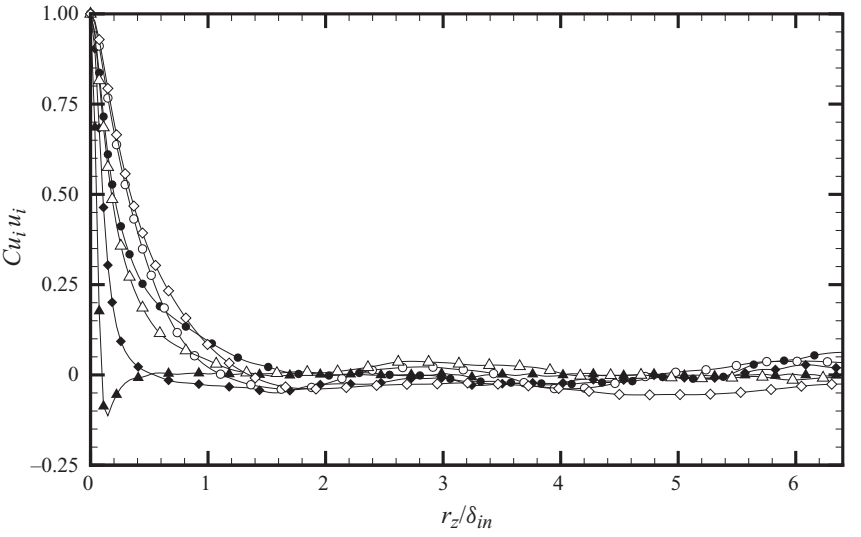

FIGURE 3. Distribution of the two-point correlation coefficient of velocity components in the spanwise direction (data taken at $x/\delta_{in} = 53.4$). Solid symbols: $y/\delta_{in} = 0.051$; open symbols: $y/\delta_{in} = 1.65$. Circles: $i = 1$; triangles: $i = 2$; diamonds: $i = 3$.

layer within a short distance from the inflow, and it allows control of the skin friction and the thickness of the simulated boundary layer.

The inflow conditions are specified according to

$$\left.\begin{aligned} \rho(0, y, z, t) &= \overline{\rho}(y) + \rho'(0, y, z, t), \\ u(0, y, z, t) &= \overline{u}(y) + u'(0, y, z, t), \\ v(0, y, z, t) &= \overline{v}(y) + v'(0, y, z, t), \\ w(0, y, z, t) &= w'(0, y, z, t), \\ p(0, y, z, t) &= p_\infty, \end{aligned}\right\} \tag{2.4}$$

where the mean velocity distribution is prescribed as suggested by Guarini *et al.* (2000), the pressure is assumed to be uniform and the mean density is determined from the Crocco–Busemann integral (White 1974). To avoid numerical 'drift' phenomena (Sagaut *et al.* 2004), the mean field at the inflow is kept constant, and only density and velocity fluctuations are recycled to the inflow. The rescaling procedure is applied by dividing the boundary layer into two sublayers: (i) the inner layer (superscript 'inn') where velocity is assumed to scale in wall coordinates ($y^+ = y/\delta_v$) and (ii) the outer layer (superscript 'out') where flow properties scale in outer units ($Y = y/\delta$, δ being the local boundary-layer thickness). The fluctuation of a generic quantity (φ) is assumed to be a weighted combination of the inner- and outer-layer fluctuations

$$\varphi = \varphi^{inn}(1 - W(Y)) + \varphi^{out}\, W(Y), \tag{2.5}$$

where the weight function $W(Y)$ is defined as (Lund *et al.* 1998)

$$W(Y) = \frac{1}{2}\left\{1 + \frac{\tanh\left[\dfrac{\alpha(Y-b)}{(1-2b)Y+b}\right]}{\tanh(\alpha)}\right\}, \tag{2.6}$$

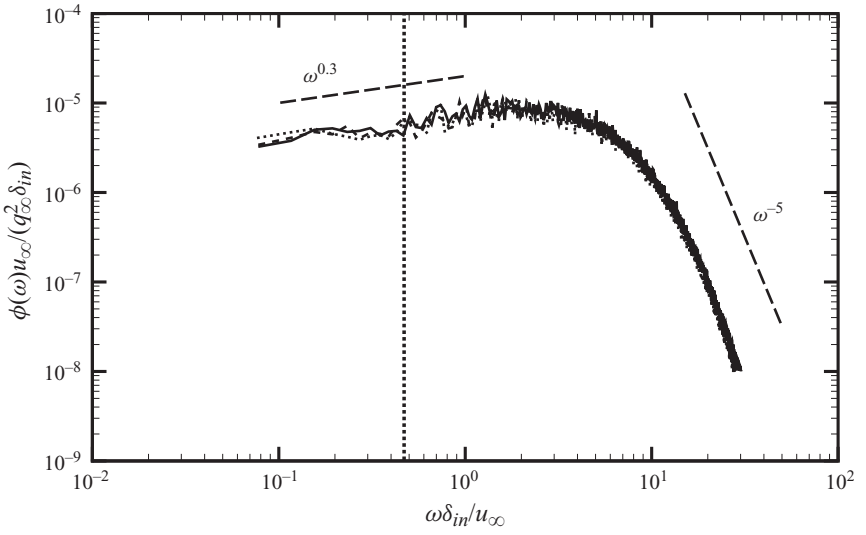

FIGURE 4. Computed wall pressure spectra at $x/\delta_{in} = 4.3$ (——); $x/\delta_{in} = 8.5$ (- - - -); $x/\delta_{in} = 12.8$ (· · · · ·). The vertical line identifies the frequency (ω_{rec}) that would be typical of phase locking (if any) associated with the recycling procedure.

with $\alpha = 4$ and $b = 0.2$. The inflow density and velocity fluctuations in each sublayer are rescaled from the recycling station (x_{rec}) according to

$$\left.\begin{array}{l} \rho'|^{inn}(0, y^+, z, t) = \rho'(x_{rec}, y^+, z + L_z/2, t), \\ u_i'|^{inn}(0, y^+, z, t) = \gamma\, u_i'(x_{rec}, y^+, z + L_z/2, t), \\ \rho'|^{out}(0, Y, z, t) = \rho'(x_{rec}, Y, z + L_z/2, t), \\ u_i'|^{out}(0, Y, z, t) = \gamma\, u_i'(x_{rec}, Y, z + L_z/2, t), \end{array}\right\} \tag{2.7}$$

where γ is the rescaling parameter:

$$\gamma = \frac{(u_\tau \sqrt{\overline{\rho}_w})_{in}}{(u_\tau \sqrt{\overline{\rho}_w})_{rec}}. \tag{2.8}$$

To minimize spurious time periodicity that may result from the application of quasi-periodic boundary conditions in the streamwise direction, the recycling station is set at $x_{rec} = 10.68\,\delta_{in}$, and the inflow fluctuations at the spanwise location z are rescaled from a staggered location ($z + L_z/2$) at the recycling station (Spalart, Strelets & Travin 2006). Random divergence-free disturbances with maximum amplitude $4\,\%\,u_\infty$ are also added at the inflow to break any remaining symmetry.

To assess the validity of the numerical inflow conditions, in figure 4 we report the computed two-sided frequency power spectra of the wall pressure, normalized by the free-stream dynamic pressure ($q_\infty = 1/2\,\rho_\infty u_\infty^2$), at various streamwise stations upstream of the interaction zone ($x/\delta_{in} = 4.3, 8.5, 12.8$) as a function of the angular frequency (ω). All pressure spectra exhibit a maximum at $\omega \approx 3\,u_\infty/\delta_{in}$, and have a shape similar to the one found in low-speed boundary layers (Na & Moin 1998*b*), with a low-frequency power-law scaling as $\omega^{0.3}$ and a high-frequency roll-off as ω^{-5}. No spectral peak associated with phase locking deriving from the recycling procedure is observed. If present, such a peak would occur at $f_{rec} \approx u_c/x_{rec}$, where $u_c \approx 0.8\,u_\infty$ is the typical convection velocity of pressure disturbances inside the boundary layer (Bull 1967), and this would correspond to $\omega_{rec} \approx 0.48\,u_\infty/\delta_{in}$ (indicated with a vertical line

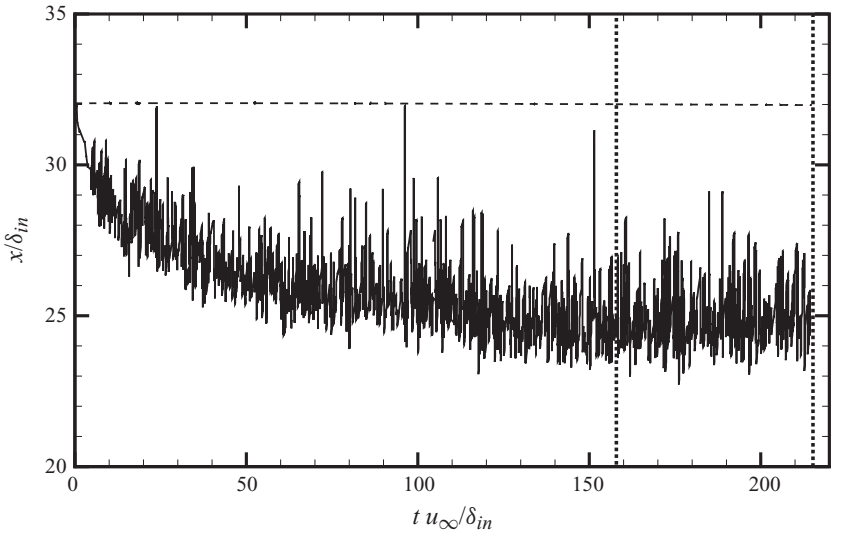

FIGURE 5. Time evolution of the maximum pressure gradient locations at the wall (solid line) and at the upper boundary (dashed line). The vertical lines indicate the initial and the final time for the collection of flow samples.

in figure 4). This implies that no significant statistical correlation develops between turbulent fluctuations at the inflow and the recycling station.

The boundary conditions at the no-slip adiabatic wall are enforced by prescribing zero wall-normal gradient for temperature and pressure, and homogeneous Dirichlet boundary conditions for all velocity components. Non-reflecting boundary conditions are specified both at the outflow and at the upper boundaries to inhibit spurious reflections of disturbances back into the computational domain (Poinsot & Lele 1992). Periodic boundary conditions are used in the spanwise direction to exploit homogeneity of the flow.

The flow field is initialized by assuming a mean turbulent boundary layer with superposed deterministic perturbations mimicking inner- and outer-layer coherent structures (Pirozzoli *et al.* 2008). The flow properties are suitably redefined past the initial shock location by enforcing a jump in density, velocity and pressure corresponding to a normal shock wave with upstream Mach number $M_0 = 1.3$. The calculation is advanced in time by monitoring the distribution of the wall friction coefficient and the position of the maximum pressure gradient at the upper and lower walls, whose time evolution is reported in figure 5. The use of non-reflecting boundary conditions, coupled with grid stretching in the streamwise direction, effectively avoids the feedback of pressure disturbances from the outflow (with subsequent drift of the interacting shock) over the time interval of the simulation. Indeed, the upper part of the shock is observed to move by less than one grid cell over the time interval of the calculation, whereas the location of maximum wall pressure gradient first moves to the left, due to an upstream influence mechanism, and then starts to oscillate around a nearly constant value, once statistical steadiness is achieved (after a time interval $T_0\,u_\infty/\delta_{in} \approx 158$). Samples of the flow field are periodically stored at time intervals of $\Delta t\,u_\infty/\delta_{in} \approx 0.18$, up to the final time $T_f\,u_\infty/\delta_{in} \approx 220$. The statistical properties of the flow (convergence of flow statistics up to third order was carefully checked) are

M_e	Re_θ	Re_{δ_2}	Re_τ	C_f	δ^*/δ	θ/δ	H	H_i
1.3	1161	932	359	3.90×10^{-3}	0.219	0.101	2.18	1.44

TABLE 1. Properties of incoming boundary layer at the reference station $x_{ref} = 17.3\,\delta_{in}$. $M_e = u_e/c_e$; $Re_\theta = \rho_e\, u_e\theta/\mu_e$; $Re_{\delta_2} = \rho_e\, u_e\theta/\mu_w$; $Re_\tau = \rho_w\, u_\tau\delta/\mu_w$; $C_f = 2\tau_w/(\rho_e\, u_e^2)$; $H = \delta^*/\theta$; $H_i = \delta_i^*/\theta_i$.

determined by taking time averages of the flow samples and assuming homogeneity in the spanwise direction.

3. Results and discussion

3.1. *Characterization of incoming boundary layer*

The turbulence statistics and the structure of the incoming flow are first compared to those of a canonical zero-pressure-gradient (ZPG) boundary layer. For this purpose we analyse the boundary layer at the reference station $x_{ref} = 17.3\,\delta_{in}$, chosen immediately upstream of the beginning of the interaction (see figure 2). The global boundary-layer properties at this location are listed in table 1. The thickness of the boundary layer (δ) is determined as the point where $\overline{u} = 0.99\,u_e$, and the displacement (δ^*) and momentum (θ) thicknesses are defined as

$$\delta^* = \int_0^{\delta_e} \left(1 - \frac{\overline{\rho}}{\rho_e}\frac{\overline{u}}{u_e}\right) \mathrm{d}y, \tag{3.1}$$

$$\theta = \int_0^{\delta_e} \frac{\overline{\rho}}{\rho_e}\frac{\overline{u}}{u_e}\left(1 - \frac{\overline{u}}{u_e}\right) \mathrm{d}y, \tag{3.2}$$

where δ_e is the edge of the rotational part of the flow field, and u_e and ρ_e are the corresponding 'external' mean velocity and density. The 'incompressible' boundary-layer thicknesses (δ_i^* and θ_i) and the associated shape factor (H_i) are also determined from (3.1) and (3.2) by setting the density ratio to unity.

The distribution of the Van Driest transformed mean streamwise velocity

$$u_{vd} = \int_0^{\overline{u}} \left(\frac{\overline{\rho}}{\overline{\rho}_w}\right)^{1/2} \mathrm{d}\overline{u} \tag{3.3}$$

at the reference station is reported in figure 6 in inner scaling, together with the incompressible boundary-layer DNS data of Wu & Moin (2009) at $Re_\theta = 900$ ($Re_\tau = 400$) and Spalart (1988) at $Re_\theta = 670$ ($Re_\tau = 280$). The agreement between the incompressible distributions and the transformed velocity is satisfactory, especially in the inner layer. A linear scaling, expected in the case of adiabatic boundary-layer flows (Smits & Dussauge 2006), is recovered for $y^+ \leqslant 5$, and a narrow overlap region, characterized by a nearly logarithmic scaling, is observed for $40 \leqslant y^+ \leqslant 100$. The strength of the wake component, defined as the difference between the Van Driest velocity and the log-law value at the boundary-layer edge, is found to be 1.18, consistent with the correlations of Fernholz & Finley (1980) at similar values of $Re_{\delta_2} = \rho_e\, u_e\theta/\mu_w$.

Consistent with Morkovin's hypothesis (Morkovin 1961), the density-scaled turbulence intensities (reported in figure 7 in inner (a) and outer (b) coordinates) match well (especially in the inner layer) with incompressible DNS data (Spalart 1988; Wu & Moin 2009) and low-speed boundary-layer experiments (Erm & Joubert

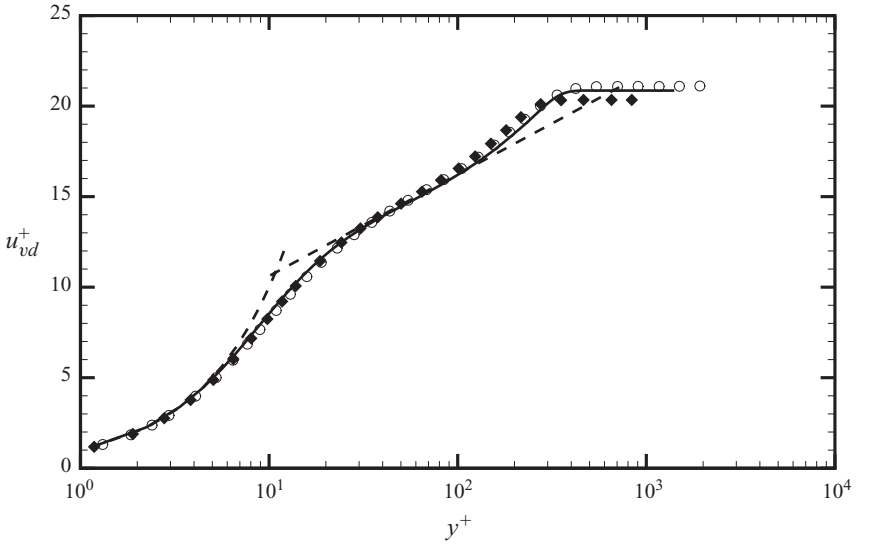

FIGURE 6. Distribution of the Van Driest transformed mean streamwise velocity in inner scaling at the reference station ($x_{ref} = 17.3\,\delta_{in}$). Solid line: present DNS; open circles: Wu & Moin (2009); diamonds: Spalart (1988); dashed lines: $u^+_{vd} = y^+$ and $u^+_{vd} = 5.0 + 1/0.41 \log y^+$.

1991). In particular, the figure shows that the streamwise velocity fluctuation peaks at about 13 wall units from the wall, where it attains a value of 2.7.

3.2. *Mean wall properties*

The mean wall pressure ($\overline{p}_w$) across the interaction zone is compared with the experimental data of Délery & Marvin (1986) and Bruce (2008). Note that the former were obtained in a transonic channel with a wall-mounted bump to accelerate the flow and form a supersonic region terminated by a quasi-normal shock wave. Hence, due to the presence of the bump, the boundary layer upstream of the shock wave develops under a favourable pressure gradient, and it exhibits a fuller profile than in a ZPG boundary layer at the same Reynolds number. As a consequence, the wall pressure distribution is not constant upstream of the interaction, and the incompressible shape factor has a relatively small value (see table 2). Because of the differences in the Reynolds numbers, and the sensitivity of the flow details to the downstream conditions, comparison with experiments should be interpreted in only a qualitative sense.

Let the interaction length scale L be defined as the distance between the sonic point location x_s (i.e. the streamwise station where the mean wall pressure equals the critical pressure) and the origin of the interaction x_0 (i.e. the point where the wall pressure starts to rise and attains the value $\overline{p}_w = 1.005\,p_\infty$). For weak-to-moderate interactions, Délery & Marvin (1986) showed that L scales with the upstream boundary-layer properties according to

$$L \approx 70\,\delta_0^*\,(H_{i0} - 1)\,. \tag{3.4}$$

As observed in table 2, the computed interaction length scale agrees fairly well with (3.4); the significant deviations observed for the data of Bruce (2008) are presumably related to three-dimensional effects in the experimental arrangement (Bruce & Babinsky 2009). Délery & Marvin (1986) also showed collapse of the wall properties

	M_0	Re_{θ_0}	H_{i_0}	L/δ_0^*	$L/\delta_0^*/(H_{i_0}-1)$	Symbol
DNS	1.3	1215	1.44	28.4	64.5	—
Délery & Marvin (1986)	1.3	7526	1.30	21.0	70.0	●
Bruce (2008)	1.28	11 590	1.36	35.0	97.0	△

TABLE 2. Interaction parameters for DNS and experiments (the subscript 0 refers to the origin of the interaction).

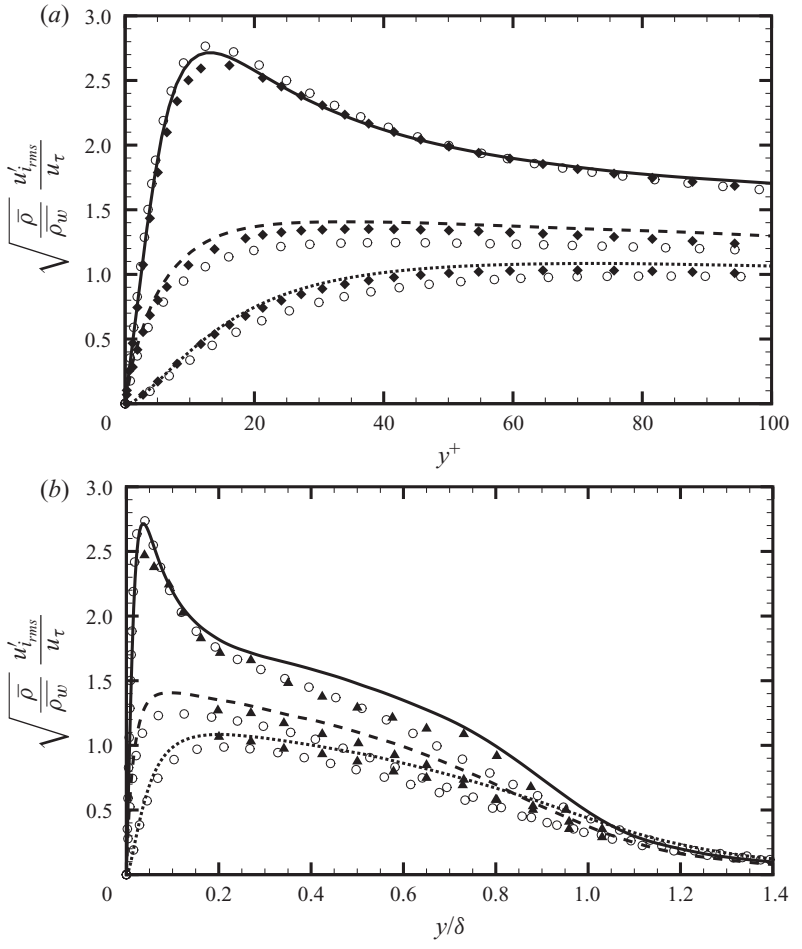

FIGURE 7. Density-scaled turbulence fluctuations in inner scaling (*a*) and outer scaling (*b*) at the reference station ($x_{ref} = 17.3\,\delta_{in}$). Lines refer to DNS data: solid line, streamwise component ($i = 1$); dotted line, wall-normal component ($i = 2$); dashed line, spanwise component ($i = 3$). Symbols: open circles, Wu & Moin (2009); diamonds, Spalart (1988); triangles, Erm & Joubert (1991).

(at various Re and M) when reported in the scaled interaction coordinates $x^* = (x - x_0)/L$, $y^* = y/L$. In the following, for comparison purposes, the results are then reported in terms of x^*, y^*, and we refer to three distinct zones: the upstream ZPG region ($x^* < 0$); the supersonic adverse-pressure-gradient (APG) region ($0 \leqslant x^* \leqslant 1$); and the subsonic APG region ($x^* > 1$).

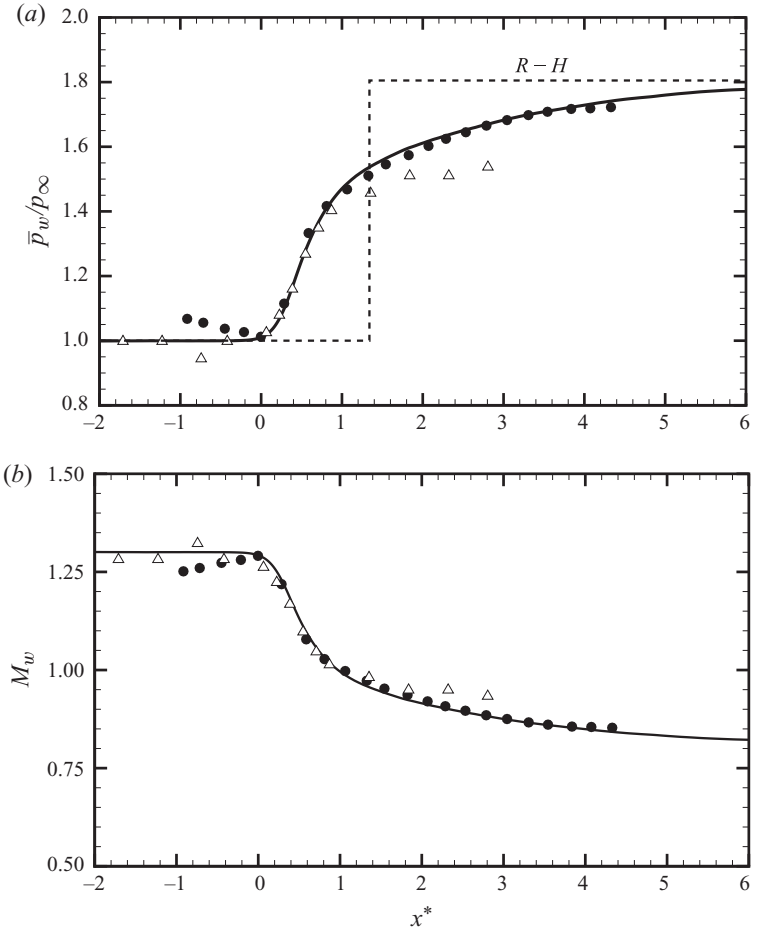

FIGURE 8. Distribution of mean wall pressure (a) and isentropic wall Mach number (b). $R-H$ denotes the inviscid distribution resulting from the Rankine–Hugoniot jump conditions. Refer to table 2 for nomenclature of symbols.

The mean wall pressure (see figure 8a) exhibits a sharp rise in the supersonic APG region, in agreement with experiments, and a milder increase in the subsonic APG region. The 'isentropic' Mach number, i.e. the Mach number corresponding to the local mean wall pressure through the isentropic relations (see figure 8b) obviously follows an opposite behaviour, and it compares well with the data of Délery & Marvin (1986).

3.3. *Boundary-layer development*

To characterize the spatial evolution of the boundary layer across the interaction zone we analyse the distributions of the displacement and momentum thicknesses. Following Garnier, Sagaut & Deville (2002), in (3.1) and (3.2) the edge of the rotational part of the boundary layer (δ_e) is defined as the point where the mean spanwise vorticity becomes less than a suitable threshold value (here set to $0.005\,u_\infty/\delta_{in}$).

The distributions of δ^* and θ (normalized with respect to their value at the origin of the interaction) and of the incompressible shape factor ($H_i = \delta_i^*/\theta_i$) are reported in figure 9 as a function of x^*. Upstream of the interaction H_i varies between

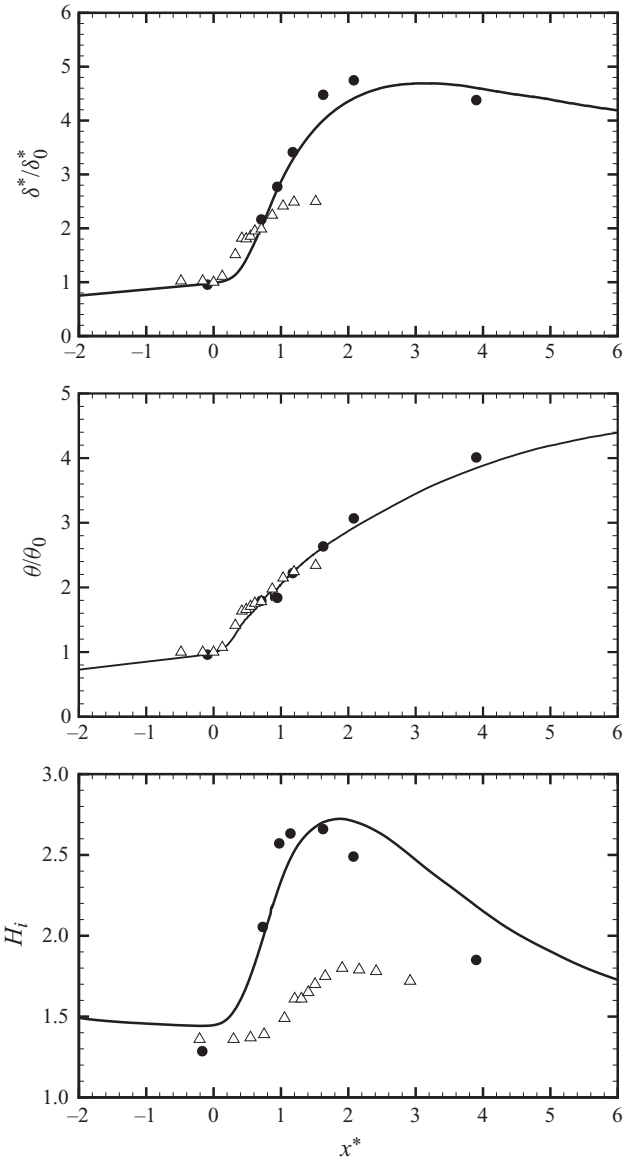

FIGURE 9. Evolution of boundary-layer properties across the interaction zone. For nomenclature of symbols see table 2.

1.44 and 1.5, as in the case of low-Reynolds-number canonical boundary layers (Wu & Moin 2009). Past the origin of the interaction ($x^* \geqslant 0$), the displacement thickness increases, attaining a maximum value of $\delta^*/\delta_0^* = 4.5$ at $x^* \approx 2.8$, whereas the momentum thickness exhibits a continuous increase, the flow not being separated in the mean (Délery & Marvin 1986). Due to bulk flow compression, the flow is retarded (as reflected in a steep rise of H_i), thus leading to the formation of a pair of inflection points past $x^* \approx 0.3$ (as observed at stations 3–7 in figure 10). The boundary layer undergoes a relaxation process past $x^* \approx 1.8$, where H_i attains a peak, and this is not yet completed at the end of the (well-resolved part of the) computational domain.

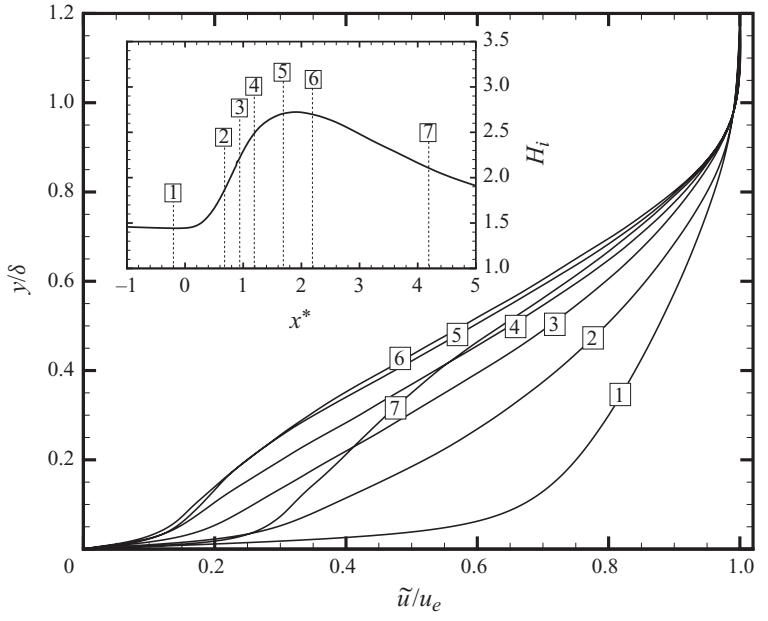

FIGURE 10. Mean velocity profiles at various streamwise stations, normalized by local boundary-layer thickness (δ) and local mean external velocity (u_e). [1] $x^* = -0.2$; [2] $x^* = 0.68$; [3] $x^* = 0.94$; [4] $x^* = 1.19$; [5] $x^* = 1.69$; [6] $x^* = 2.19$; [7] $x^* = 4.19$.

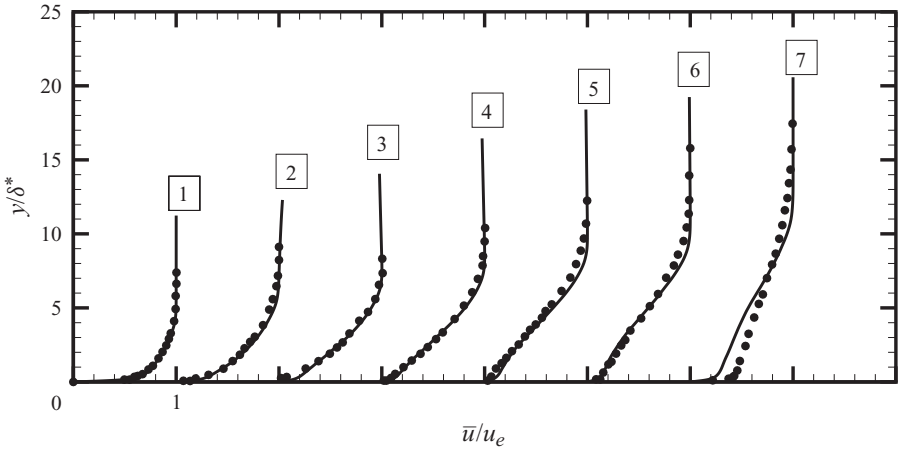

FIGURE 11. Mean velocity profiles at various streamwise stations, compared with the data of Délery & Marvin (1986). For nomenclature, refer to figure 10.

Comparison of the mean velocity profiles across the interaction zone with the experimental data of Délery & Marvin (1986) is reported in figure 11. The discrepancies observed at station 7 are to be ascribed either to differences in the rate of the relaxation process (which is expected to be slower at lower Reynolds number) or to differences in the downstream flow conditions.

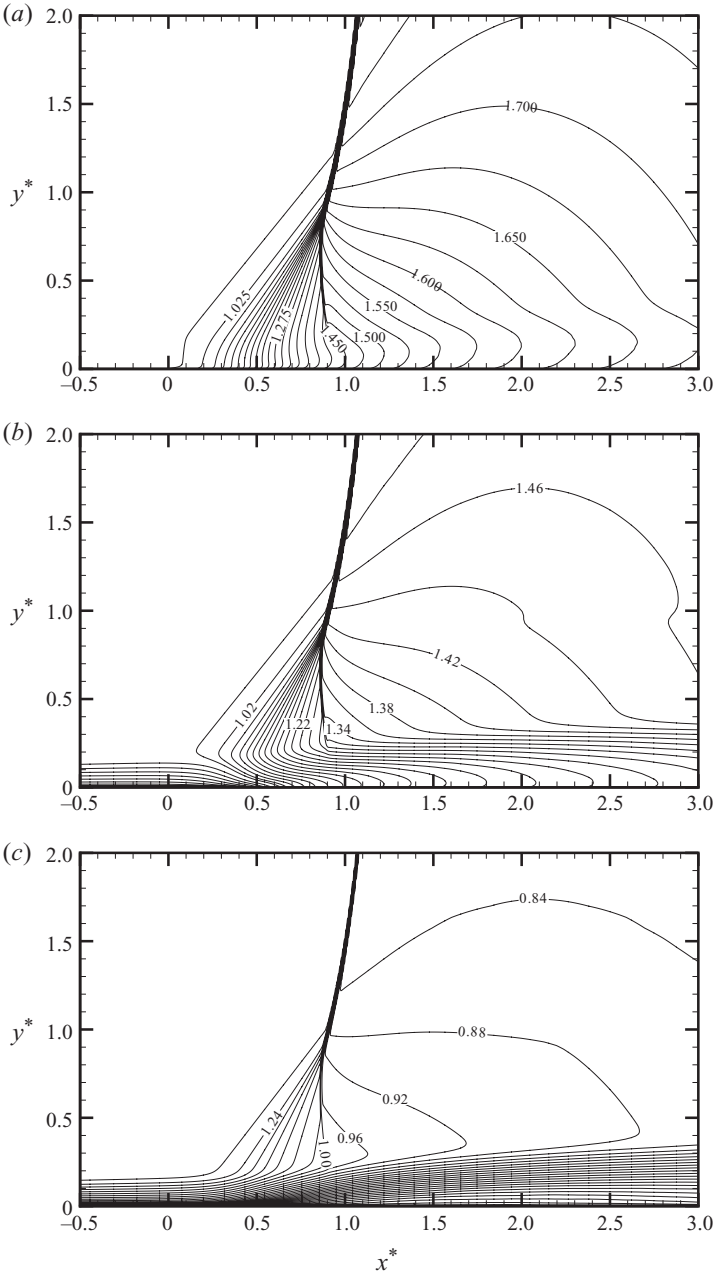

FIGURE 12. Mean fields of pressure $\overline{p}/p_\infty$ (*a*), density $\overline{\rho}/\rho_\infty$ (*b*) and Mach number (*c*) in the streamwise, wall-normal plane.

3.4. *Flow visualizations: mean and instantaneous fields*

The iso-contour lines of the mean pressure, density and Mach number are reported in figure 12, which shows a pattern consistent with previous experimental observations (East 1976; Délery & Marvin 1986). The shock system consists of the interacting shock, which is observed to bend significantly while approaching the wall, and a fan of compression waves originated well upstream of the nominal impingement

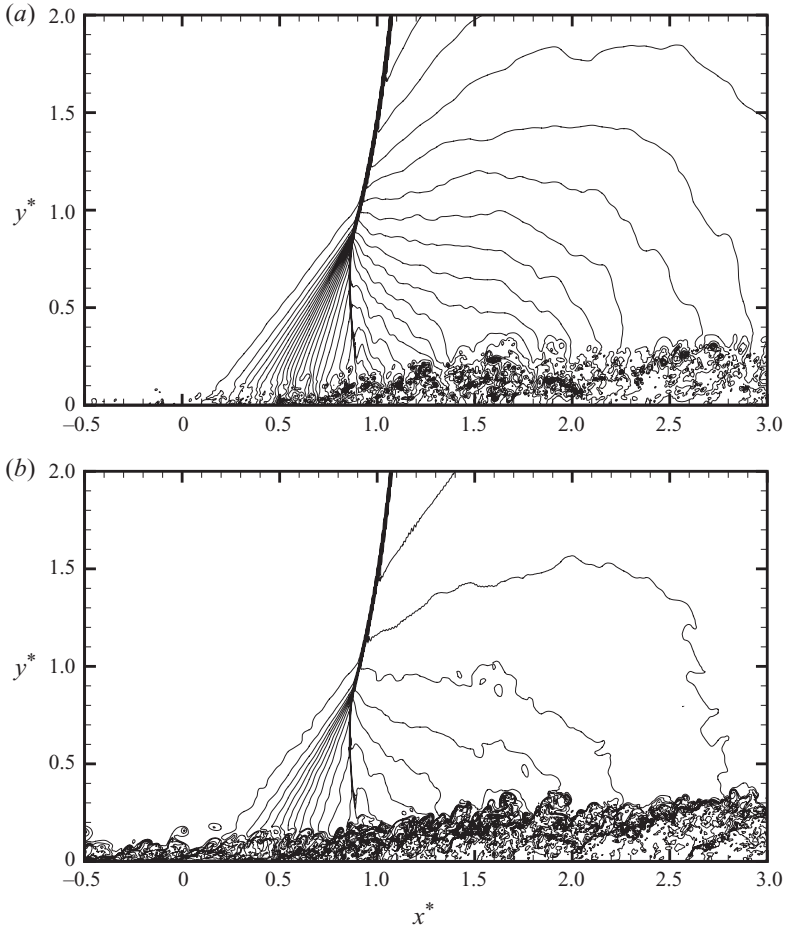

FIGURE 13. Instantaneous fields of pressure p/p_∞ (a) and density ρ/ρ_∞ (b) in the streamwise, wall-normal plane: (a) 44 contour levels, from 0.96 to 1.84; (b) 32 contour levels, from 0.77 to 1.53. Supplementary movie 1 of the pressure field is available at journals.cambridge.org/flm.

point, and it is terminated by a nearly normal trailing shock. The location of the wall sonic point nearly coincides with the foot of the rear shock, and the 'triple point' lies at $y^* \approx 0.9$. Downstream of the rear shock the flow is fully subsonic, and no supersonic tongue is observed. The formation of a mixing layer (associated with the outermost mean velocity inflection points in figure 10) is also visible in the mean pressure and density fields, which exhibit a dip past the interaction region at a distance $y^* = 0.1$–0.2 from the wall.

The computed instantaneous pressure and density fields are reported in figure 13 in the streamwise, wall-normal plane at a given time frame. As observed by Pirozzoli & Grasso (2006) in the case of an impinging shock/boundary layer interaction at supersonic Mach number, and by Na & Moin (1998*a*) for a low-speed turbulent boundary layer under APG, the instantaneous pressure field highlights the formation of pressure minima associated with the shedding of eddies that form in the proximity of the outermost inflection points of the mean velocity profiles. As better appreciated from inspection of the flow animations, such vortices lift off from the

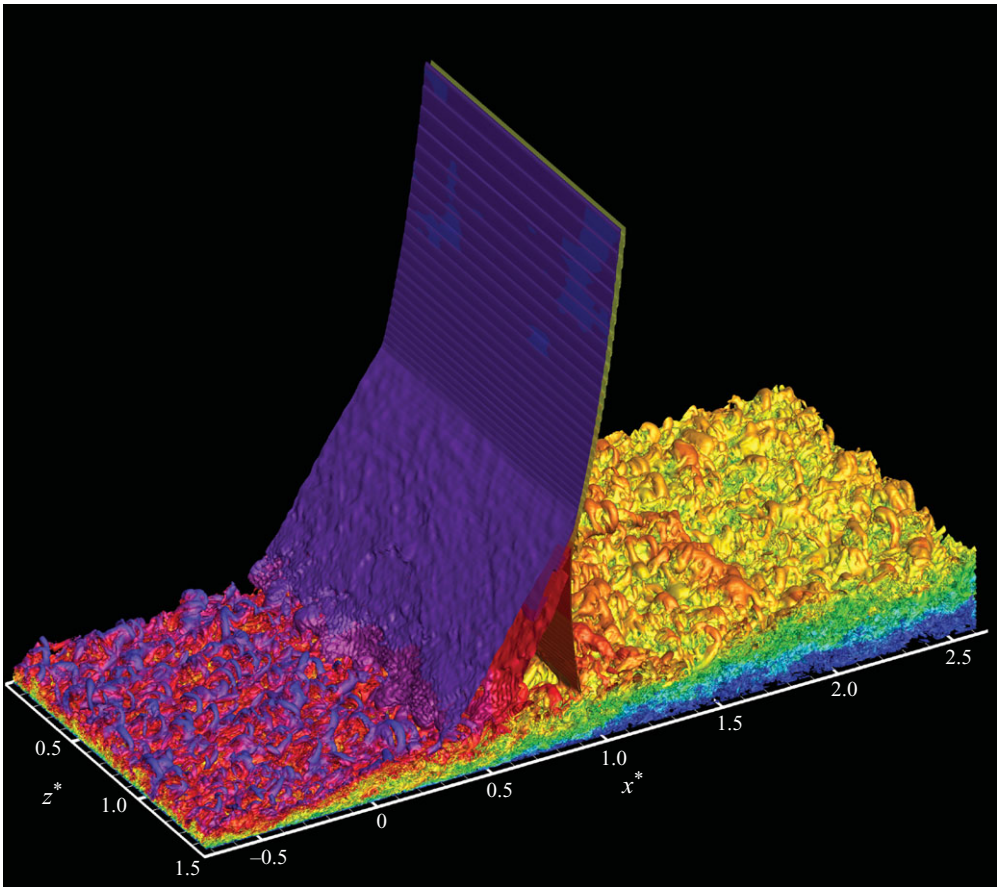

FIGURE 14. Iso-surfaces of pressure gradient modulus in the proximity of the interaction zone. Three levels are shown: $|\nabla p|\,\delta_{in}/p_\infty = 0.05, 0.16, 0.29$, coloured with the local Mach number (levels from 0 to 1.3, blue to violet).

wall approximately in the middle of the interaction zone and propagate downstream, giving rise to a turbulent mixing layer. Sharp density interfaces are also observed in the outermost part of the boundary layer, separating boundary-layer turbulence from the outer, essentially inviscid flow, and this becomes more convoluted past the interaction zone.

For a more complete representation of the flow, in figure 14 we report a three-dimensional instantaneous view of the SBLI region in terms of iso-surfaces of the pressure gradient modulus. Such an indicator allows detection at the same time of compression and expansion zones (for obvious reasons), as well as vortical structures, corresponding to regions of low pressure. The figure highlights the three-dimensional nature of the lambda-like interaction pattern, whereby the vortical structures in the incoming boundary layer cause the spanwise wrinkling of the upstream compression fan, as observed by Wu & Martin (2007) in the case of a supersonic compression ramp interaction. Numerous hairpin-shaped vortex loops, which closely resemble those found in incompressible boundary-layer DNS (Wu & Moin 2009), are observed both in the ZPG region and past the shock wave.

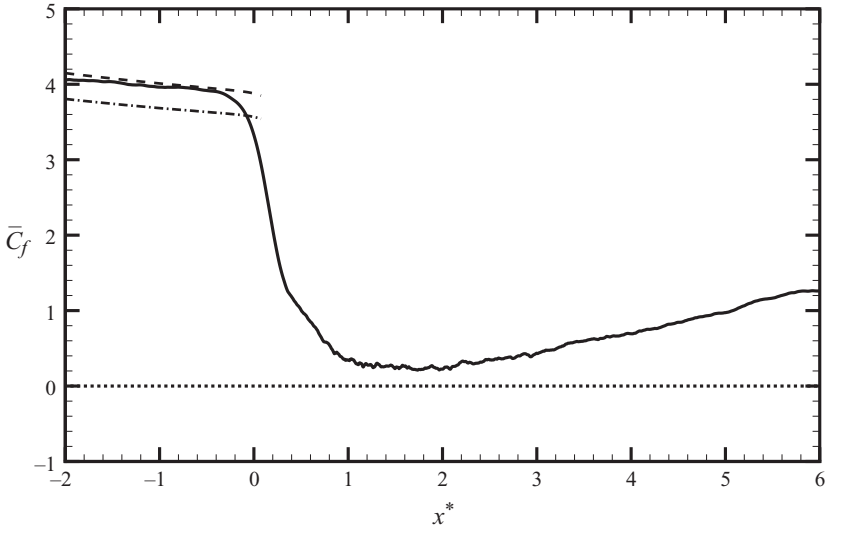

FIGURE 15. Distribution of mean skin friction coefficient: ——, DNS; - · - · -, Kármán–Schoenherr (see (3.5)); – – – –, Blasius (see (3.6)).

3.5. *Analysis of flow reversal*

The distribution of the average skin friction coefficient $\overline{C}_f = \tau_w/q_\infty$ is shown in figure 15, where we also report (for the ZPG region) the incompressible skin friction correlations of Kármán–Schoenherr:

$$C_{f_i} = 1/(17.08\,(\log_{10} Re_{\theta i})^2 + 25.11\,\log_{10} Re_{\theta i} + 6.012), \tag{3.5}$$

and Blasius

$$C_{f_i} = 0.026/Re_{\theta_i}^{1/4}. \tag{3.6}$$

As customary for compressible flows (Hopkins & Inouye 1971), the Van Driest II transformation is used (here written for an adiabatic wall) to extend the skin friction correlations to compressible flow conditions

$$C_{f_i} = F_c\,C_f, \quad Re_{\theta i} = F_\theta\,Re_\theta, \tag{3.7}$$

where

$$F_c = \frac{\overline{T}_w/T_\infty - 1}{\arcsin^2\alpha}, \quad F_\theta = \frac{\mu_\infty}{\overline{\mu}_w}, \quad \alpha = \frac{\overline{T}_w/T_\infty - 1}{\sqrt{\overline{T}_w/T_\infty\,(\overline{T}_w/T_\infty - 1)}}.$$

Upstream of the interaction, the DNS data fall very close to the Blasius curve, with deviations of $O(5\,\%)$ from the Kármán–Schoenherr's relation. Starting at about $x^* = 0$, the skin friction exhibits a drop, and it attains a minimum in the subsonic region past the shock ($x^* \approx 1.8$), followed by a slow recovery.

To characterize the intermittency and unsteady separation of the flow, we have analysed the statistical probability of wall points with locally reversed flow ($\overline{\gamma}$) and the instantaneous skin friction coefficient in the wall plane, reported in figures 16 and 17, respectively. According to the classification of Simpson (1989), incipient detachment (ID) occurs with instantaneous backflow 1 % of the time, intermittent transitory detachment (ITD) occurs with instantaneous backflow 20 % of the time and transitory detachment (TD, which in practice coincides with mean detachment) with 50 % probability of instantaneous backflow. The streamwise distribution of

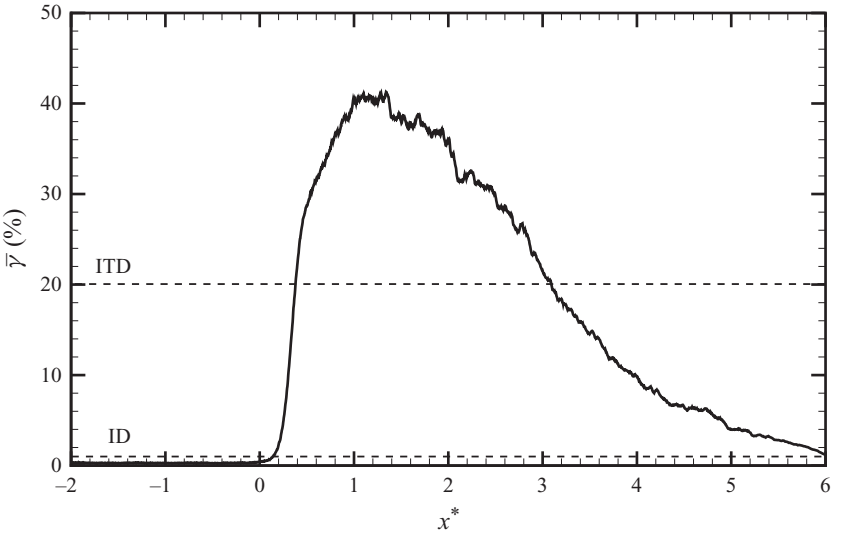

FIGURE 16. Distribution of statistical probability of wall points with $\partial u/\partial y < 0$. ID: incipient detachment; ITD: intermittent transitory detachment.

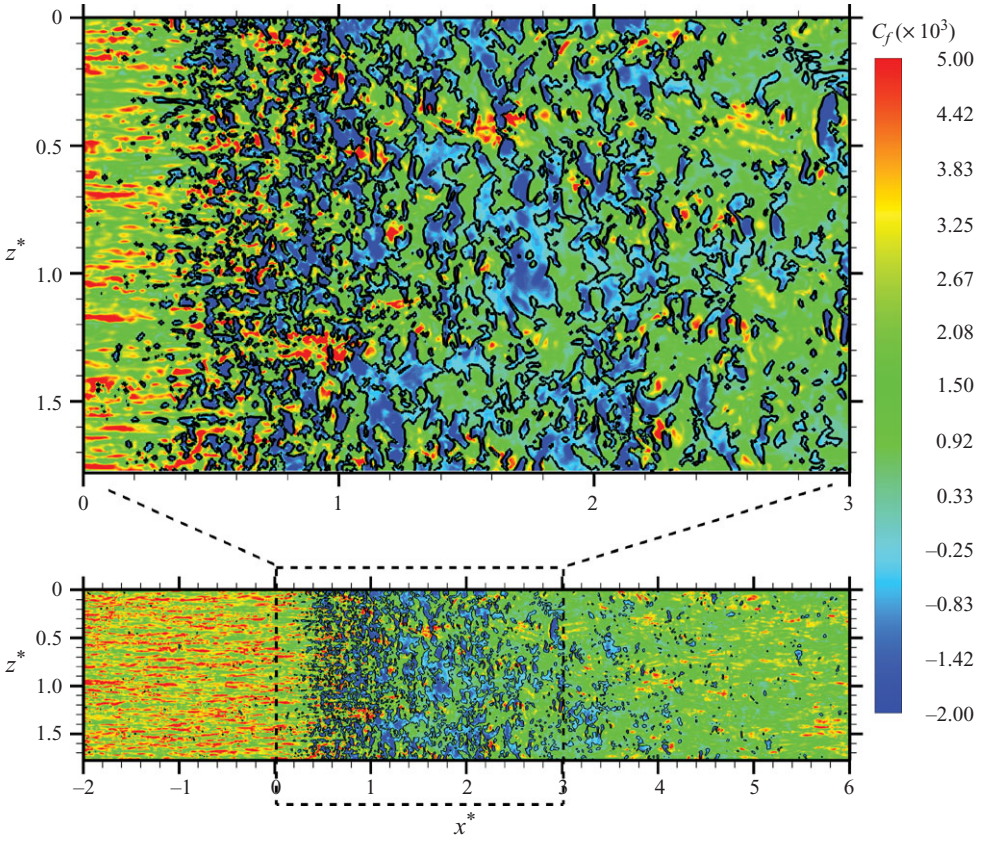

FIGURE 17. Contours of instantaneous skin friction (the iso-line $C_f = 0$ is reported in black).

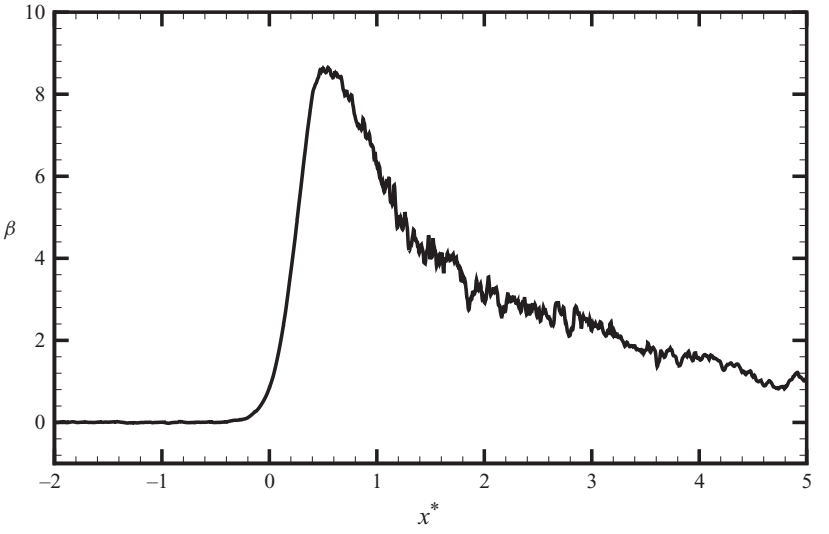

FIGURE 18. Distribution of Clauser's pressure gradient parameter (β) as a function of the streamwise coordinate.

$\overline{\gamma}$, reported in figure 16, shows the occurrence of an extended region with ITD regime (for $0.4 \leqslant x^* \leqslant 3.1$), without any mean flow reversal. Such a regime is characterized by scattered spots of instantaneously reversed flow that exhibit a strong intermittent character (figure 17). In particular, the streaky pattern typical of the upstream ZPG boundary layer disappears due to the APG, and flow patches with negative instantaneous C_f are frequently found starting from the middle of the interaction zone, and extending well into the recovery region.

3.6. *Analysis of flow recovery*

The flow past the interacting shock is characterized by an extended region where the boundary layer rearranges to attain a new equilibrium state. To characterize such a relaxation mechanism we have in the first instance applied the classical theory of Clauser (1954). According to Clauser's analysis, equilibrium states of a boundary layer are characterized by self-similarity of the velocity defect scaled by the friction velocity (reported as a function of y/δ), and correspond to regions where the pressure gradient parameter

$$\beta = \frac{\delta^*}{\rho_w u_\tau^2} \frac{\mathrm{d}\overline{p}_w}{\mathrm{d}x} \tag{3.8}$$

is constant. The distribution of β, reported in figure 18, shows that it is (obviously) zero in the incoming boundary layer, where equilibrium is attained. The pressure gradient parameter exhibits a sharp increase at the origin of the interaction, attaining a peak in the middle of the supersonic APG zone, and decreases monotonically further downstream. Therefore, according to Clauser's definition, the flow in the recovery region is not in equilibrium, and the scaled velocity defect profiles (not reported) do not collapse onto a single curve.

Using a similarity analysis of the RANS equations, Castillo & George (2001) have proposed that the proper velocity scale for the outer layer is the external velocity u_e, rather than the friction velocity. By introducing a modified pressure gradient

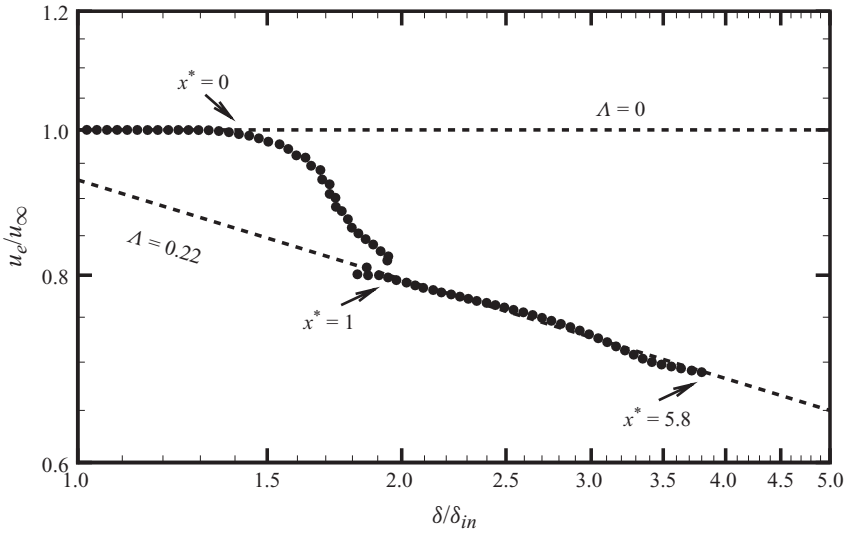

FIGURE 19. Distribution of outer velocity u_e/u_∞ as a function of δ/δ_{in}. The dashed lines denote the theoretical scalings obtained from (3.10).

parameter, defined as

$$\Lambda = \frac{\delta}{\rho_e u_e^2 \, \mathrm{d}\delta/\mathrm{d}x} \frac{\mathrm{d}\overline{p}_w}{\mathrm{d}x} = -\frac{\delta}{u_e \, \mathrm{d}\delta/\mathrm{d}x} \frac{\mathrm{d}u_e}{\mathrm{d}x}, \tag{3.9}$$

they suggested that, in the absence of mean flow separation, the admissible equilibrium states correspond to regions of constant Λ, which also implies a power-law dependence of the boundary-layer thickness upon the external velocity:

$$\delta \sim u_e^{-1/\Lambda}. \tag{3.10}$$

According to such a definition, most of the experimental data analysed by Castillo & George (2001) were found to be in equilibrium (in contrast to Clauser's analysis), and only three values of Λ were found to be possible: $\Lambda = 0.22$ (for APG), $\Lambda = 0$ (for ZPG) and $\Lambda = -1.92$ (for favourable pressure gradient). Under such conditions, the mean velocity defect profiles were found to exhibit reasonable collapse when reported in the scaling of Zagarola & Smits (1998), i.e. by normalizing the velocity defect by $u_e\delta^*/\delta$.

To verify the occurrence of equilibrium states in the recovery region of the present DNS, in figure 19 we report the distribution of the external velocity (u_e/u_∞) as a function of δ/δ_{in}. Bearing in mind (3.10), the figure reveals that the boundary layer is in equilibrium both in the ZPG region, where $\Lambda \approx 0$, and in the subsonic APG region, where $\Lambda \approx 0.22$, in excellent agreement with the findings of Castillo & George (2001). Consistently, the Van Driest velocity defect profiles in the Zagarola & Smits scaling are found to be self-similar throughout the subsonic APG region (stations 5–7 of figure 20), whereas no collapse is observed in the supersonic APG region (§§ 2–4), where the boundary layer is out of equilibrium.

3.7. *Turbulence statistics*

The structural modifications of turbulence upon interaction with the shock system are analysed in the present section. As a first check, in figure 21 we report the distributions of the streamwise turbulence intensity at various stations, which show

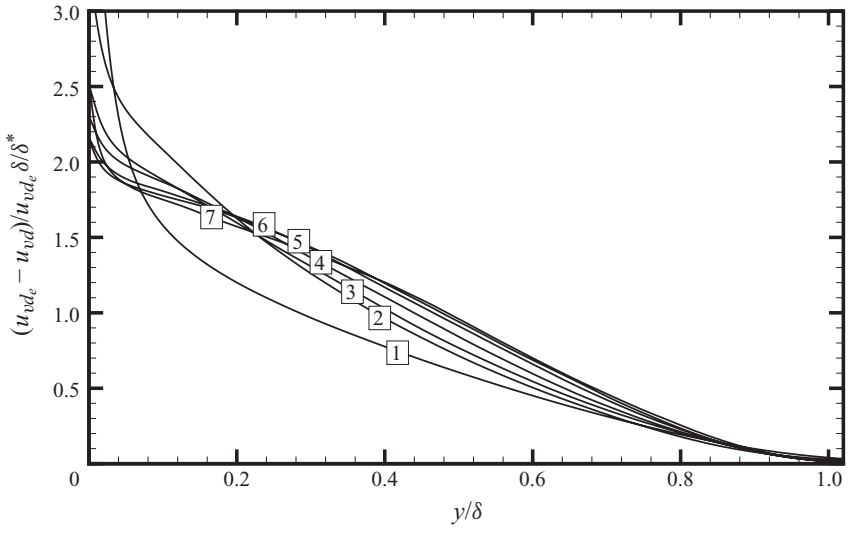

FIGURE 20. Mean velocity defect profiles at various streamwise stations in Zagarola–Smits scaling. For nomenclature, refer to figure 10.

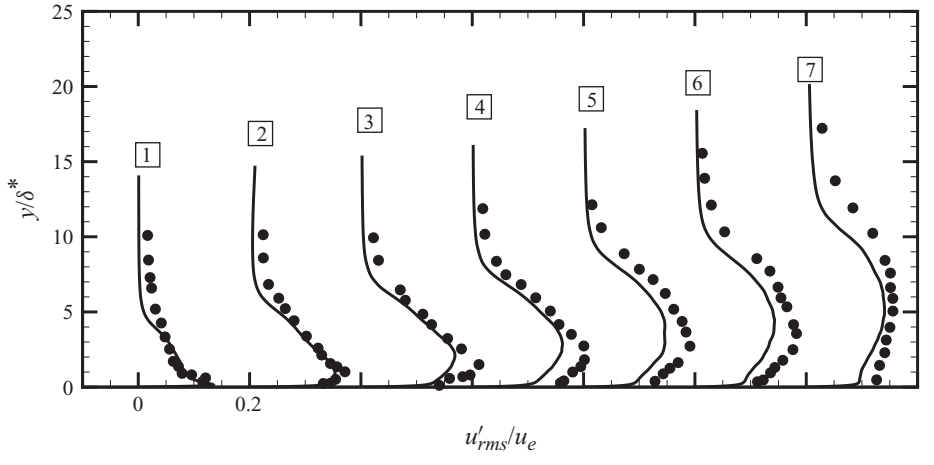

FIGURE 21. Streamwise turbulence intensities at various streamwise stations, compared with the data of Délery & Marvin (1986). For nomenclature, refer to figure 10.

good agreement with the experimental data of Délery & Marvin (1986) throughout the interaction zone. Starting from station 3, differences in the fluctuation levels of about 30 % are found, all the way through the subsonic APG zone (stations 4–7).

The iso-contour lines of the Reynolds stress components $\widetilde{u_i'' u_j''}$, in the streamwise/wall-normal plane, are shown in figure 22. (For clarity of representation the coordinate axes are not to scale.) In the figure we also report the mid-line of the mixing layer, i.e. the locus of points where the mean shear is maximum. Figure 22 shows a general amplification of Reynolds stresses in the APG region, especially in the mixing layer, where the shedding of vortical structures occurs, as also found by Délery (1983), and for supersonic interactions by Adams (2000), Pirozzoli & Grasso (2006), Wu & Martin (2007) and Touber & Sandham (2009). To get a more quantitative appreciation, in figure 23 we also report the profiles of the Reynolds

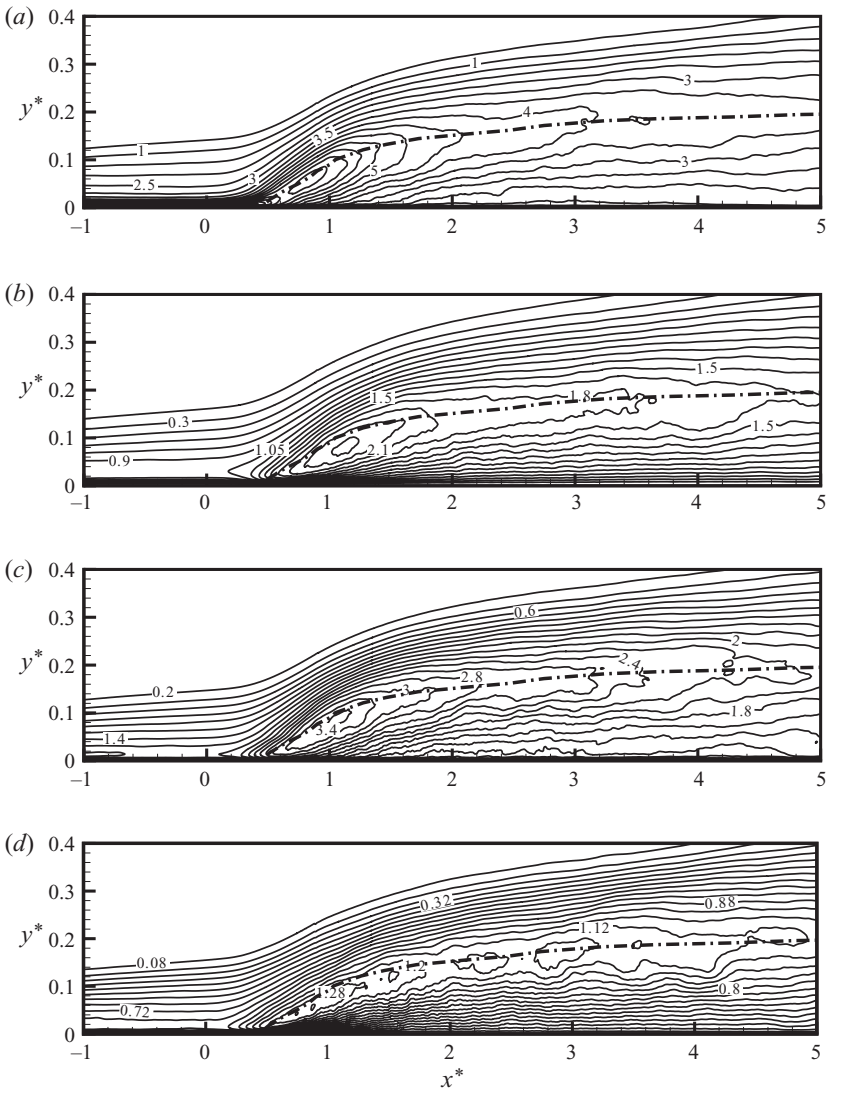

FIGURE 22. Contour plots of Reynolds stress tensor components: (*a*) $\widetilde{u''u''}/u^2_{\tau_{ref}}$; (*b*) $\widetilde{v''v''}/u^2_{\tau_{ref}}$; (*c*) $\widetilde{w''w''}/u^2_{\tau_{ref}}$; (*d*) $-\widetilde{u''v''}/u^2_{\tau_{ref}}$, where $u_{\tau_{ref}}$ is the friction velocity at the reference station ($x_{ref} = 17.3\,\delta_{in}$). The chained line denotes the mid-line of the mixing layer.

stress components in the wall-normal direction at various streamwise stations. The figure shows substantially different amplification of the Reynolds stress components through the supersonic APG region. Specifically, while the streamwise turbulence intensity is relatively unaffected, the turbulent shear stress and the cross-stream velocity fluctuations experience an approximately twofold increase with respect to their upstream levels. For instance, at station 3 (just past the end of the supersonic APG region), the stress components $-\widetilde{u''v''}$, $\widetilde{v''v''}$ and $\widetilde{w''w''}$ are amplified by a factor of about 1.6, 2.2 and 1.9, respectively. In the subsonic APG region ($x^* > 1$), where the mixing layer undergoes a continuous spreading, all Reynolds stress components undergo a monotonic decay, and their peak locations consistently move away from the

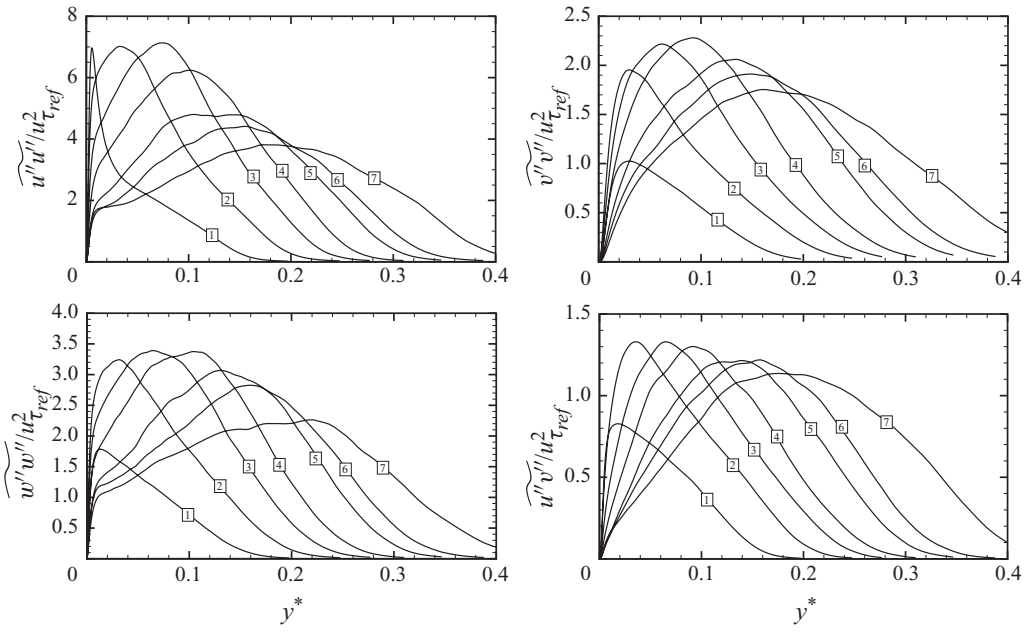

FIGURE 23. Reynolds stress tensor components at various streamwise stations. For nomenclature, refer to figure 10.

wall. The structure parameter $-\widetilde{u''v''}/k$ (not reported) attains values of approximately 0.3 in the ZPG region, dropping to values in the range 0.2–0.3 past the origin of the interaction.

To better characterize the change in anisotropy of the Reynolds stress tensor (which is a consequence of the different amplification undergone by its individual components) in the APG region, we have considered the invariants of the stress anisotropy tensor

$$b_{ij} = \frac{\widetilde{u_i''u_j''}}{2k} - \frac{1}{3}\delta_{ij}. \tag{3.11}$$

Since b_{ij} has zero trace by definition, a representative picture of the turbulence state is provided by its second and third invariants:

$$III = b_{ij}b_{jk}b_{ki}, \quad II = b_{ij}b_{ji}. \tag{3.12}$$

As shown by Lumley (1978), all realizable fields must lie inside the anisotropy invariant map, whose vertices constitute special states of turbulence. The computed anisotropy invariant maps at various streamwise stations are reported in figure 24. In the ZPG region (station 1), a nearly two-component turbulence state is observed in the proximity of the wall, due to its blocking effect; the maximum anisotropy is attained in the buffer layer ($y^+ \approx 10$), with a return to isotropy in the outer layer, as observed in the case of canonical boundary-layer flow (Pope 2000). Throughout the APG region (enclosed between stations 2 and 7), turbulence attains a two-component, axisymmetric state in the immediate vicinity of the wall. In the inner part of the boundary layer ($y/\delta \leqslant 0.1$) the anisotropy of the flow is reduced with respect to the ZPG state, and most turbulence states fall close to the line corresponding to the axisymmetric turbulence compression. Due to the APG experienced through the interaction, the mean shear is reduced, thus promoting

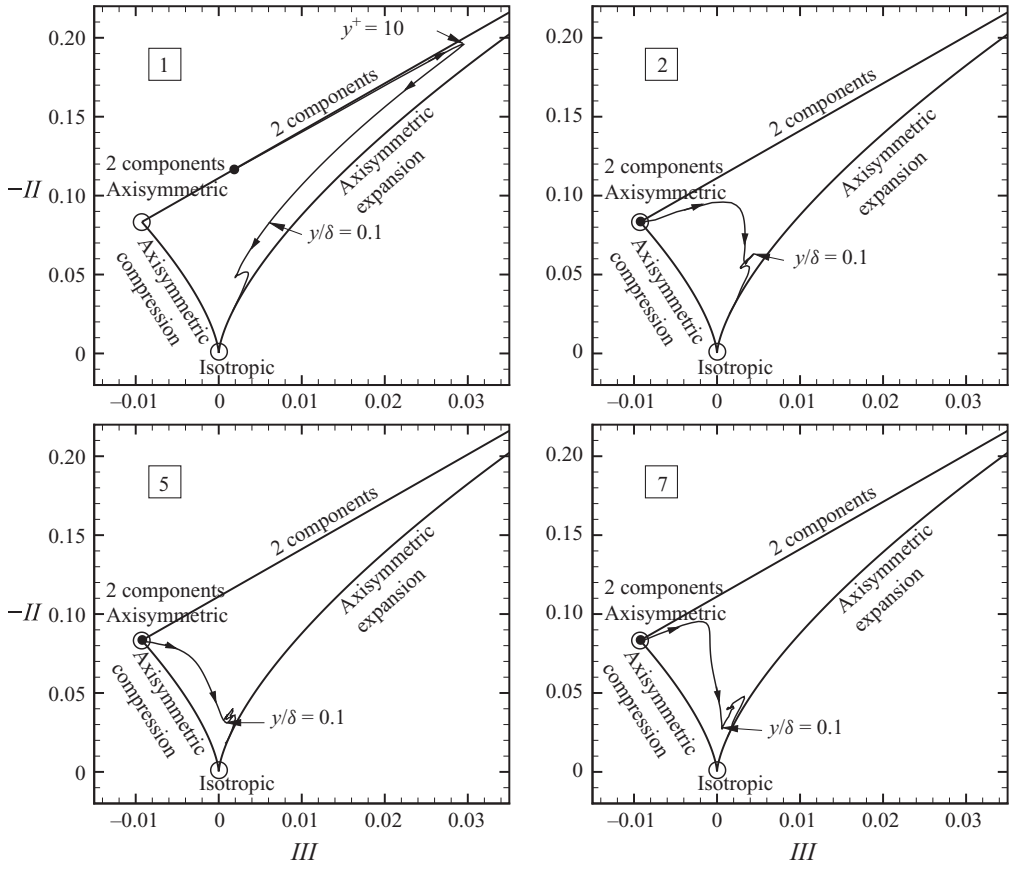

FIGURE 24. Anisotropy invariant maps of the Reynolds stress tensor in the boundary layer at various streamwise locations (refer to figure 10 for nomenclature). Filled circles denote wall points and arrows indicate the direction of increasing y.

equipartition of turbulence fluctuations in the wall-parallel plane and tendency to the 'isotropization' of turbulence. In the outer region ($y/\delta \geqslant 0.1$) turbulence attains an axisymmetric expansion turbulence state, as observed at the centre of canonical turbulent mixing layers (Pope 2000). Farther downstream (station 7) turbulence shows a reversal tendency, experiencing an increase of anisotropy in the near-wall region. This scenario is qualitatively confirmed by visual inspection of figure 25, where we report the streamwise velocity field in a wall-parallel plane (at $y^+ = 10.8$ in wall units evaluated at the reference station $x_{ref} = 17.3\,\delta_{in}$). The figure shows the presence of elongated streaks with alternating high- and low-speed fluids in the ZPG region, which penetrate into the APG region, and disappear past $x^* \approx 0.5$. Farther downstream, turbulence exhibits a more 'isotropic' behaviour, and a tendency for streaks to reform is observed for $x^* \gtrsim 5$. This tendency is also quantitatively supported by figure 26, where we report the streamwise distribution of the shear rate parameter $\widetilde{S} = -(\widetilde{u''v''}\,\partial\tilde{u}/\partial y)/\varepsilon$ (where ε is the dissipation rate of turbulence kinetic energy, to be defined in (3.18)), at $y^+_{ref} = 10.8$ (wall units being evaluated at the reference station). This parameter was introduced by Lam & Banerjee (1992) to identify the condition of streak formation in a wall-bounded turbulent flow. They showed that streaks appear when turbulence production due to mean shear exceeds

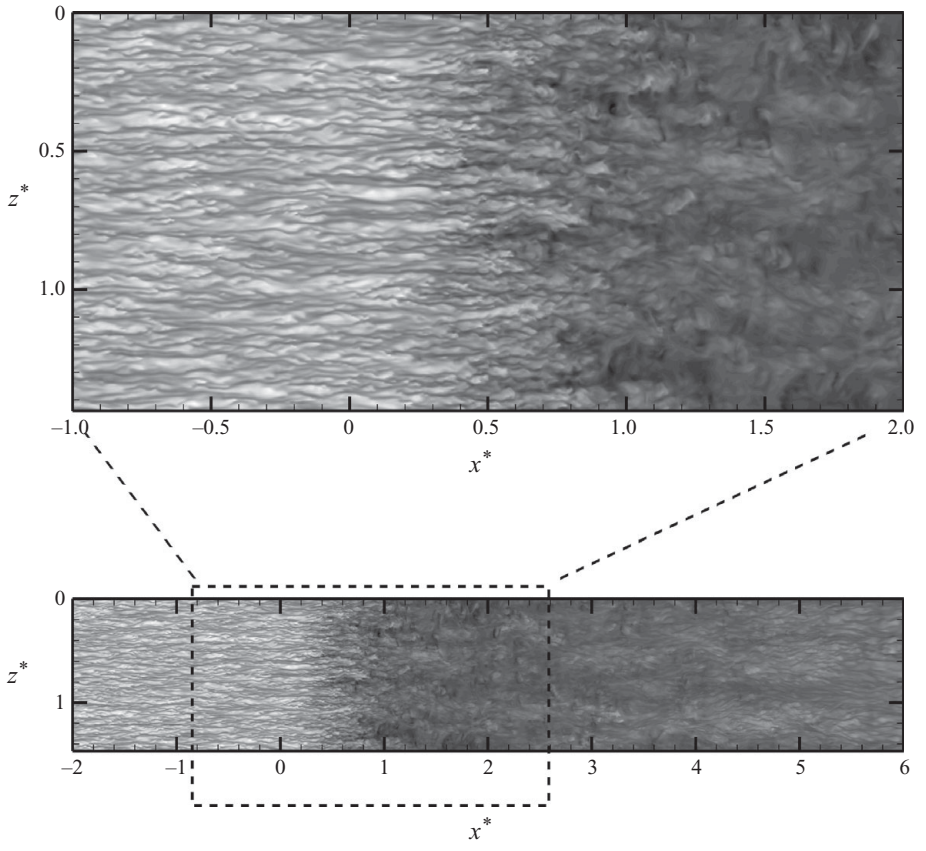

FIGURE 25. Distribution of the streamwise velocity component in a wall-parallel plane at $y^+ = 10.8$ (wall units taken at x_{ref}): $-0.13 \leqslant u/u_\infty \leqslant 0.78$, 36 equally spaced levels, from black to white.

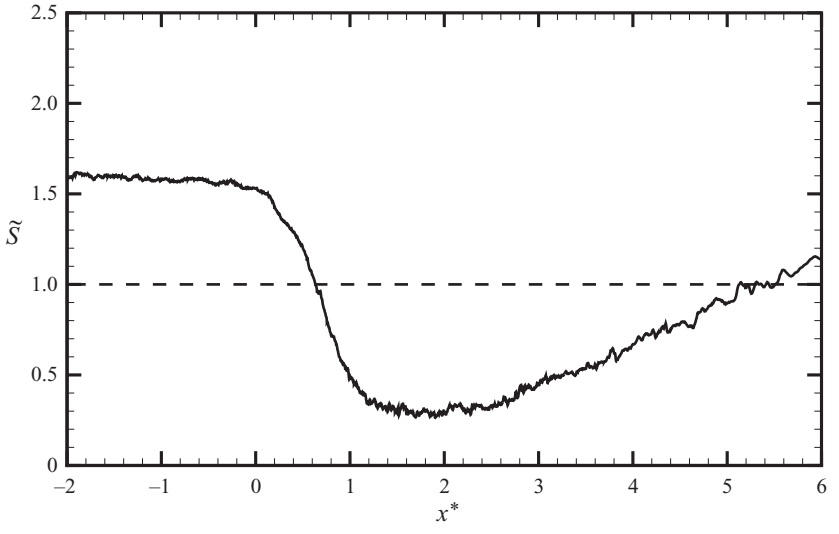

FIGURE 26. Streamwise distribution of the non-dimensional shear rate parameter $\widetilde{S}$ at $y^+_{ref} = 10.9$. Wall units are defined in terms of flow properties at the reference station ($x^* = 17.3\,\delta_{in}$) of the incoming boundary layer.

viscous dissipation, i.e. when $\widetilde{S} \geqslant 1$. Our results indicate that $\widetilde{S}$ is nearly constant (≈ 1.5) in the ZPG region, and it decays rapidly in the supersonic APG region, because of the reduction of the mean shear. It then undergoes a gradual recovery in the subsonic APG region, exceeding unity again towards the end of the computational domain ($x^* \geqslant 5$).

3.8. *Turbulence kinetic energy budgets*

Useful information for improving RANS turbulence models can be gained from the analysis of the turbulence kinetic energy budgets. The transport equation for turbulence kinetic energy ($k = (1/2)\widetilde{u_i'' u_i''}$) in a compressible flow is cast in the form (Pirozzoli, Grasso & Gatski 2004)

$$\frac{\partial \overline{\rho} k}{\partial t} = C + T + P + V - \overline{\rho}\varepsilon + K, \tag{3.13}$$

where C, T, P, V and $\overline{\rho}\varepsilon$, respectively, represent the contributions of mean advection, turbulent transport, production by mean velocity gradient, viscous diffusion and viscous dissipation. The term K accounts for the direct effect of compressibility through pressure–dilatation correlation and mass diffusion. The explicit expressions for the various terms are as follows:

$$C = -\frac{\partial \overline{\rho}\tilde{u}_j k}{\partial x_j}, \tag{3.14}$$

$$T = -\frac{\partial}{\partial x_j}\left[\frac{1}{2}\overline{\rho}\,\widetilde{u_i'' u_i'' u_j''} + \overline{p' u_j''}\right], \tag{3.15}$$

$$P = -\overline{\rho}\,\widetilde{u_i'' u_j''}\,\frac{\partial \tilde{u}_i}{\partial x_j}, \tag{3.16}$$

$$V = \frac{\partial}{\partial x_j}(\overline{\sigma_{ij}' u_i''}), \tag{3.17}$$

$$\overline{\rho}\varepsilon = \overline{\sigma_{ij}' \frac{\partial u_i''}{\partial x_j}}, \tag{3.18}$$

$$K = \overline{p' \frac{\partial u_i''}{\partial x_i}} + \overline{u_i''}\left(\frac{\partial \overline{\sigma}_{ij}}{\partial x_j} - \frac{\partial \overline{p}}{\partial x_i}\right). \tag{3.19}$$

Figure 27 shows the budgets of k (normalized by wall units at the reference station $x_{ref} = 17.3\delta_{in}$) at various streamwise positions, as a function of the wall distance; the compressibility term is not shown in the figure, it being always negligible with respect to the other ones. Throughout the flow domain the terms on the right-hand side of (3.19) are balanced with good accuracy (the maximum imbalance being 6 % throughout the interaction zone), thus confirming the accurate resolution of the present simulation. In the ZPG region ($x^* = -0.2$), the budgets are typical of a canonical boundary layer, with a balance of production and dissipation in a large part of the boundary layer. Turbulence transport and viscous diffusion become significant in the near-wall region, whereas the contribution of advection is negligible. In the supersonic APG region ($x^* = 0.68$) the near-wall budget is similar to that of a canonical boundary layer, whereas differences are observed away from the wall ($y^+_{ref} \geqslant 50$), where the advection term (associated with the lift-up of vortical

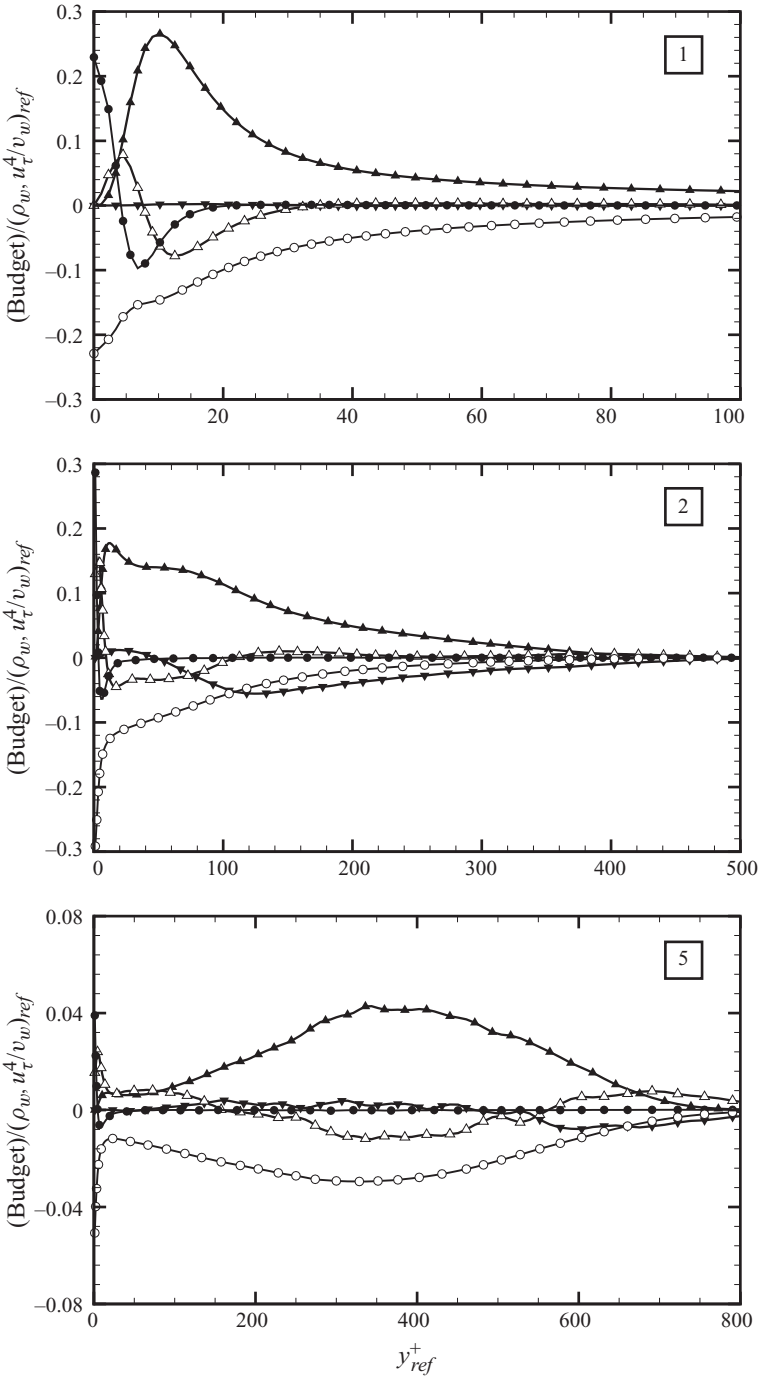

FIGURE 27. Turbulence kinetic energy balance in wall units (taken at the reference station) at various streamwise locations (refer to figure 10 for nomenclature). Symbols: ▲, production; ○, dissipation; ●, viscous diffusion; △, turbulent transport; ▼, advection.

structures) becomes significant, and it contributes to balance the mean velocity gradient production. A qualitatively different behaviour is observed in the subsonic APG region ($x^* = 2.19$), where the budget exhibits similarities with an incompressible

boundary layer under APG (Na & Moin 1998*a*), and this resembles the canonical mixing layer budget (Rogers & Moser 1993). In particular the production by mean velocity gradient peaks at ($y^+_{ref} \approx 400$), and it is balanced by turbulent transport and molecular dissipation.

4. Conclusions

The interaction of a normal shock wave with a turbulent boundary layer at $M_\infty = 1.3$, $Re_\theta \approx 1200$ has been analysed by means of DNS of the compressible Navier–Stokes equations. The study has focused on the analysis of the unsteadiness associated with the development of the vortical structures in the boundary layer, and detailed flow statistics have been reported, including mean flow properties, turbulent fluctuations, as well as second-moment budgets.

The DNS data are compared against experimental measurements in transonic channels, and satisfactory agreement is found for mean pressure, velocity profiles and turbulence intensities. Consistent with experimental observations, the mean flow pattern shows bending of the interacting shock, the formation of an upstream fan of compression waves associated with the thickening of the boundary layer and the occurrence of a terminating nearly normal shock, which brings the flow to subsonic conditions. Flow visualization shows that the outer part of the boundary layer is populated by hairpin-shaped vortical structures, both in the incoming stream and past the interacting shock, where the mean velocity profile exhibits a pair of inflection points, and the flow shows similarities with a turbulent mixing layer. Although at the selected flow conditions no mean separation is observed, the flow is in an 'ITD' state, exhibiting scattered spots of instantaneous flow reversal throughout the interaction zone.

Three distinct flow regions have been identified: (i) a ZPG region upstream of the origin of the interaction; (ii) a supersonic APG region, where the interaction between the shock and boundary-layer turbulence takes place; and (iii) a subsonic APG region, where the flow relaxes to an equilibrium state.

The analysis of the flow recovery past the interacting shock shows that the boundary layer reacts to the APG by attaining a new equilibrium state over a scale of the order of one interaction length. Such an equilibrium state is conveniently described in the framework of the theory of Castillo & George (2001). In particular, in the subsonic APG region, a nearly constant value of the pressure gradient parameter is attained, and the mean velocity defect profiles are very nearly self-similar when reported in the scaling of Zagarola & Smits (1998).

In the supersonic APG region the main effect of the interacting shock on turbulence is a general amplification of Reynolds stresses, associated with the formation of vortical structures along the mid-line of the mixing layer. However, while the cross-stream velocity fluctuations and the shear stress are significantly amplified, the streamwise velocity fluctuations are relatively unaffected, resulting in a reduction of the turbulence anisotropy, whose macroscopic effect is the suppression of the near-wall streaks of the incoming boundary layer. In the subsonic APG region, a monotonic decay of all Reynolds stress components is observed, associated with the spreading of the mixing layer. Low-speed streaks start to reform at a distance of approximately five interaction length scales past the interacting shock, where turbulence production by mean shear exceeds viscous dissipation.

This study then confirms the potential of DNS for the understanding of compressible turbulent flows in APG. Given the relative simplicity of the geometrical

configuration, we expect that it also provides a useful database for the development of improved turbulence models. Data are available upon request from the authors.

The support of the CASPUR computing consortium through the 2009 Competitive HPC Grant 'Extremely large scale simulation of transonic turbulent flows' is gratefully acknowledged. The authors wish to thank J. Délery, H. Babinsky and P. J. K. Bruce for helpful discussions, and the anonymous referees for help in improving the quality of the manuscript.

Supplementary movies are available at journals.cambridge.org/flm

REFERENCES

Adams, N. A. 2000 Direct simulation of the turbulent boundary layer along a compressible ramp at $M = 3$ and $Re_\theta = 1685$. *J. Fluid Mech.* **420**, 47–83.

Atkin, C. J. & Squire, L. C. 1992 A study on the interaction of a normal shock wave with a turbulent boundary layer at Mach numbers between 1.30 and 1.55. *Eur. J. Mech.* B/*Fluids* **11**, 93–118.

Barakos, G. & Drikakis, D. 2000 Investigation of nonlinear eddy-viscosity turbulence models in shock/boundary layer interaction. *AIAA J.* **38**, 461–469.

Batten, P., Craft, T. J., Leschziner, M. A. & Loyau, H. 1999 Reynolds-stress-transport modeling for compressible aerodynamics applications. *AIAA J.* **37**, 785–797.

Bruce, P. J. K. 2008 Transonic shock/boundary layer interactions subject to downstream pressure perturbations. PhD thesis, Magdalene College, Department of Engineering, University of Cambridge.

Bruce, P. J. K. & Babinsky, H. 2008 Unsteady shock wave dynamics. *J. Fluid Mech.* **603**, 463–473.

Bruce, P. J. K. & Babinsky, H. 2009 Behaviour of unsteady transonic shock/boundary layer interactions with three-dimensional effects. *AIAA Paper* 2009-1590.

Bull, M. K. 1967 Wall pressure fluctuations associated with subsonic turbulent boundary layer flow. *J. Fluid Mech.* **28**, 719–754.

Castillo, L. & George, W. K. 2001 Similarity analysis for turbulent boundary layer with pressure gradient: outer flow. *AIAA J.* **39**, 41–47.

Clauser, F. H. 1954 Turbulent boundary layers in adverse pressure gradients. *J. Aerosp. Sci.* **21**, 91–108.

Davidson, L. 1995 Reynolds stress transport modelling of shock-induced separated flow. *Comput. Fluids* **24**, 253–268.

Délery, J. 1983 Experimental investigation of turbulence properties in transonic shock/boundary layer interactions. *AIAA J.* **21**, 180–185.

Délery, J. & Marvin, J. G. 1986 Shock-wave boundary layer interactions. *AGARDograph* 280.

Dolling, D. S. 2001 Fifty years of shock-wave/boundary layer interaction research: what next? *AIAA J.* **39**, 1517–1531.

East, L. F. 1976 The application of a laser anemometer to the investigation of shock wave boundary layer interactions. *AGARD-CPP* 193.

Erm, L. P. & Joubert, J. 1991 Low Reynolds number turbulent boundary layers. *J. Fluid Mech.* **230**, 1–44.

Fernholz, H. H. & Finley, P. J. 1980 A critical commentary on mean flow data for two-dimensional compressible turbulent boundary layers. *AGARDograph* 253.

Garnier, E., Sagaut, P. & Deville, M. 2002 Large-eddy simulation of shock/boundary-layer interaction. *AIAA J.* **40** (10), 1935–1944.

Gerolymos, G. A. & Vallet, I. 1997 Near-wall Reynolds-stress three-dimensional transonic flow computation. *AIAA J.* **35**, 228–236.

Guarini, S. E., Moser, R. D., Shariff, K. & Wray, A. 2000 Direct numerical simulation of a supersonic boundary layer at Mach 2.5. *J. Fluid Mech.* **414**, 1–33.

Hopkins, E. J. & Inouye, M. 1971 An evaluation of theories for predicting turbulent skin friction and heat transfer on flat plates at supersonic and hypersonic Mach numbers. *AIAA J.* **9**, 993–1003.

Jiang, G. S. & Shu, C. W. 1996 Efficient implementation of weighted ENO schemes. *J. Comput. Phys.* **126**, 202.

Jiménez, J. & Wray, A. A. 1998 On the characteristics of vortex filaments in isotropic turbulence. *J. Fluid Mech.* **373**, 255–285.

Knight, D., Yana, H., Panaras, A. G. & Zheltovodov, A. 2003 Advances in CFD prediction of shock wave turbulent boundary layer interactions. *Prog. Aerosp. Sci.* **39**, 121–184.

Lam, K. & Banerjee, S. 1992 On the condition of streak formation in a bounded turbulent flow. *Phys. Fluids* **4** (2), 306–320.

Leschziner, M. A., Batten, P. & Loyau, H. 2000 Modelling shock-affected near-wall flows with anisotropy-resolving turbulence closures. *Intl J. Heat Fluid Flow* **21**, 239–251.

Leschziner, M. A. & Drikakis, D. 2002 Turbulence modelling and turbulent-flow computation in aeronautics. *Aeronaut. J.* **106**, 349–384.

Liu, X. & Squire, L. C. 1988 An investigation of shock/boundary-layer interactions on curved surfaces at transonic speeds. *J. Fluid Mech.* **187**, 467–486.

Lumley, J. L. 1978 Computational modeling of turbulent flows. *Adv. Appl. Mech.* **18**, 123–176.

Lund, T. S., Wu, X. & Squires, K. D. 1998 Generation of turbulent inflow data for spatially-developing boundary layer simulations. *J. Fluid Mech.* **140**, 233–258.

Morkovin, M. V. 1961 Effects of compressibility on turbulent flows. In *Mécanique de la Turbulence* (ed. A. Favre), p. 367. CNRS.

Na, Y. & Moin, P. 1998*a* Direct numerical simulation of a separated turbulent boundary layer. *J. Fluid Mech.* **374**, 379–404.

Na, Y. & Moin, P. 1998*b* The structure of wall-pressure fluctuations in turbulent boundary layers with adverse pressure gradient and separation. *J. Fluid Mech.* **377**, 347–373.

Pirozzoli, S. 2002 Conservative hybrid compact-WENO schemes for shock–turbulence interaction. *J. Comput. Phys.* **178**, 81–117.

Pirozzoli, S., Bernardini, M. & Grasso, F. 2007 Aeroacoustics of transonic shock–boundary layer interactions. *AIAA Paper* 2007-3416.

Pirozzoli, S., Bernardini, M. & Grasso, F. 2008 Characterization of coherent vortical structures in a supersonic turbulent boundary layer. *J. Fluid Mech.* **613**, 205–231.

Pirozzoli, S. & Grasso, F. 2004 Direct numerical simulations of isotropic compressible turbulence: influence of compressibility on dynamics and structures. *Phys. Fluids* **16** (12), 4386–4407.

Pirozzoli, S. & Grasso, F. 2006 Direct numerical simulation of impinging shock wave turbulent boundary layer interaction at $M = 2.25$. *Phys. Fluids* **18**, 065113.

Pirozzoli, S., Grasso, F. & Gatski, T. B. 2004 Direct numerical simulation and analysis of a spatially evolving supersonic turbulent boundary layer at $M = 2.25$. *Phys. Fluids* **16** (3), 530–545.

Poinsot, T. J. & Lele, S. K. 1992 Boundary conditions for direct simulations of compressible viscous flows. *J. Comput. Phys.* **101**, 104–129.

Pope, S. B. 2000 *Turbulent Flows*. Cambridge University Press.

Rogers, M. & Moser, R. 1993 Direct numerical simulation of a self-similar turbulent mixing layer. *Phys. Fluids* A **6**, 903–923.

Sagaut, P., Garnier, E., Tromeur, E., Larcheveque, L. & Labourasse, E. 2004 Turbulent inflow conditions for large eddy simulation of compressible wall-bounded flows. *AIAA J.* **42**, 469–477.

Sandham, N. D., Yao, Y. F. & Lawal, A. A. 2003 Large-eddy simulation of transonic flow over a bump. *Intl J. Heat Fluid Flow* **24**, 584–595.

Seddon, J. 1960 The flow produced by interaction of a turbulent boundary layer with a normal shock wave of strength sufficient to cause separation. *Tech. Rep.* 3502. ARC R & M.

Simpson, R. L. 1989 Turbulent boundary layer separation. *Annu. Rev. Fluid Mech.* **21**, 205–234.

Smits, A. J. & Dussauge, J. P. 2006 *Turbulent Shear Layers in Supersonic Flow*. American Institute of Physics.

Spalart, P., Strelets, M. & Travin, A. 2006 Direct numerical simulation of large-eddy-break-up devices in a boundary layer. *Intl J. Heat Fluid Flow* **27**, 902–910.

Spalart, P. R. 1988 Direct numerical simulation of a turbulent boundary layer up to $Re_\theta = 1410$. *J. Fluid Mech.* **187**, 61–98.

Stolz, S. & Adams, N. A. 2003 Large-eddy simulation of high-Reynolds-number supersonic boundary layers using the approximate deconvolution model and a rescaling and recycling technique. *Phys. Fluids* **15**, 2398–2412.

Touber, E. & Sandham, N. D. 2009 Large-eddy simulation of low-frequency unsteadiness in a turbulent shock-induced separation bubble. *Theor. Comput. Fluid Dyn.* **23**, 79–107.

White, F. M. 1974 *Viscous Fluid Flow*. McGraw-Hill.

Wu, M. & Martin, M. P. 2007 Direct numerical simulation of supersonic turbulent boundary layer over a compression ramp. *AIAA J.* **45**, 879–889.

Wu, X. & Moin, P. 2009 Direct numerical simulation of turbulence in a nominally zero-pressure-gradient flat-plate boundary layer. *J. Fluid Mech.* **630**, 5–41.

Xu, S. & Martin, M. P. 2004 Assessment of inflow boundary conditions for compressible turbulent boundary layers. *Phys. Fluids* **16**, 2623–2639.

Zagarola, M. & Smits, A. J. 1998 Mean-flow scaling of turbulent pipe flow. *J. Fluid Mech.* **373**, 33–79.